JOURNAL OF GEOPHYSICAL RESEARCH: OCEANS, VOL. 118, 2667–2684, doi:10.1002/jgrc.20203, 2013

Numerical simulations of oceanic pCO_2 variations and interactions between Typhoon Choi-wan (0914) and the ocean

Akiyoshi Wada,[1] Meghan F. Cronin,[2] Adrienne J. Sutton,[3] Yoshimi Kawai,[4] and Masao Ishii[1]

Received 25 September 2012; revised 5 March 2013; accepted 17 April 2013; published 30 May 2013.

[1] On 19 September 2009, Typhoon Choi-wan passed ~40 km to the southeast of the Kuroshio Extension Observatory (KEO) surface mooring, located at 32.3°N, 144.5°E. We use an atmosphere-wave-ocean coupled model that incorporated an oceanic carbon equilibrium model to investigate the typhoon-induced CO_2 outgassing observed by the KEO mooring. KEO data are used to provide atmospheric surface boundary conditions for partial pressure of CO_2 (pCO_2^{air}) and to validate the numerical results. The model simulated the observed sea-level pressure variations reasonably well, although the simulated-typhoon translation was 3 h slower than the estimated best track. The simulation resulted in lower than observed sea-surface temperature (SST), sea-surface salinity (SSS), and partial pressure of surface ocean CO_2 (pCO_2^{sea}). Better agreement was found with the grid point south of the buoy that corresponded roughly to the buoy location in the simulated-typhoon reference frame. In situ observations show CO_2 outgassing during the Choi-wan's passage. Forty percent of observed outgassing was explained by decreasing pCO_2^{air} (~20 μatm), and thus, the remainder (~30 μatm) must be explained by increasing pCO_2^{sea}. The model simulated only one third of the increase in observed surface pCO_2^{sea} variation (~9.6 μatm), suggesting that not only SST but also high salinity and dissolved inorganic carbon caused by vertical turbulent mixing and horizontal advection are important in simulating surface pCO_2^{sea} variation. The simulations also reveal that surface roughness length affects surface wind asymmetry during the passage and variation in SSS and pCO_2^{sea} (~1 μatm) after the passage.

Citation: Wada, A., M. F. Cronin, A. J. Sutton, Y. Kawai, and M. Ishii (2013), Numerical simulations of oceanic pCO_2 variations and interactions between Typhoon Choi-wan (0914) and the ocean, *J. Geophys. Res. Oceans*, *118*, 2667–2684, doi:10.1002/jgrc.20203.

1. Introduction

[2] Understanding the local carbon system induced by tropical cyclones (TCs) is important for estimating the climatological impact of the TC on the annual global CO_2 effluxes. In particular, the northwestern Pacific Ocean features some of the most numerous and intense TC found globally. TC-induced CO_2 efflux is known to be determined by both physical [e.g., *Lévy et al*., 2012] and biogeochemical [*Lin*, 2012] processes. While the TC-induced biological pump does little to enhance biological carbon fixation in the context of global climate system [*Lin*, 2012], the contribution of TC-induced physical pumping to global TC-induced efflux remains uncertain [e.g., *Lévy et al*., 2012].

[3] Interactions between the ocean and TC include a variety of physical and biological processes. A TC induces sea-surface cooling [e.g., *Price*, 1981; *Wada*, 2002], variations in ocean productivity [e.g., *Subrahmanyam et al*., 2002; *Lin et al*., 2003; *Siswanto et al*., 2008], and sea-air CO_2 flux [*Bates et al*., 1998; *Nemoto et al*., 2009; *Huang and Imberger*, 2010; *Bond et al*., 2011; *Wada et al*., 2011a, 2011b]. Sea-surface cooling induced by a TC can suppress intensification of a TC [e.g., *Bender et al*., 1993; *Bender and Ginis*, 2000] by delaying the merger of discrete mesovortices [*Wada*, 2009] and damping the eddy flux of relative angular momentum in the low- to midtroposphere. In addition, previous studies have reported that sea-surface cooling results in a change in the structure of a TC particularly within the inner core [e.g., *Zhu et al*., 2004; *Wu et al*., 2005]. These various studies highlight the multidisciplinary aspects of interactions between a TC and the ocean; however, a comprehensive interdisciplinary approach is lacking. In order to understand TC-induced local carbon system and to estimate their impact on the annual global CO_2 effluxes, the comprehensive interdisciplinary approach is needed. Among various approaches, numerical-modeling

[1]Meteorological Research Institute, Japan Meteorological Agency, Tsukuba, Japan.
[2]Pacific Marine Environmental Laboratory, NOAA, Seattle, Washington, USA.
[3]Joint Institute for the Study of the Atmosphere and Ocean, University of Washington, Seattle, Washington, USA.
[4]Research Institute for Global Change, Japan Agency for Marine-Earth Science and Technology, Yokosuka, Japan.

Corresponding author: A. Wada, Meteorological Research Institute, Japan Meteorological Agency, 1-1 Nagamine, Tsukuba, Ibaraki 305-0052, Japan. (awada@mri-jma.go.jp)

2169-9275/13/10.1002/jgrc.20203

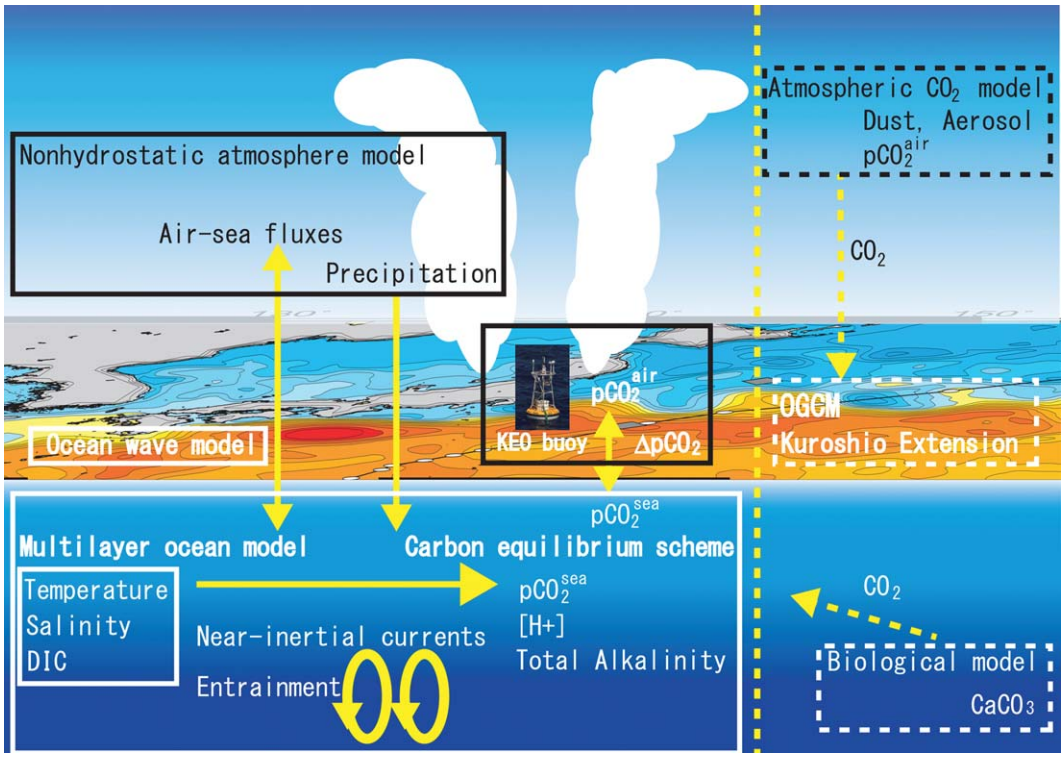

Figure 1. A schematic diagram of carbon system used or discussed in this study. The diagram of atmosphere-wave-ocean coupled model incorporating a carbon equilibrium scheme used in this study is shown on the left side of the dashed vertical line. The right side shows the components not considered in this study.

studies help understand interdisciplinary processes in both the atmosphere and the ocean.

[4] Advances in supercomputer systems enable us to study typhoon-ocean interactions numerically using a sophisticated atmosphere-ocean and physical-biochemical coupled model. Indeed, *Huang and Imberger* [2010] used a 3-D hydrostatic ocean model, Estuary, Lake and Coastal Ocean Computer Model (ELCOM), coupled with a public domain carbon model and a biochemical Computational Aquatic Ecosystem, Dynamics Model (CAEDYM) to investigate the response of the partial pressure of ocean CO_2 (pCO_2^{sea}) to the passage of Hurricane Frances in September 2004. The similar approach was conducted by *Lévy et al*. [2012], using oceanic hydrodynamic model coupled with the Pelagic Interaction Scheme for Carbon and Ecosystem Studies to study the contribution of TC on the sea-air CO_2 flux. However, these models were not coupled with both atmosphere and ocean-wave models.

[5] Modeling results should be validated by in situ observations, since numerical models contain various uncertainties due to initial conditions, parameterizations, computational errors, and unknown/unincorporated processes. However, in situ observations are scarce, particularly under the conditions of high winds and high ocean waves. *Nemoto et al*. [2009] described 3 h observations of pCO_2^{sea}, associated with the response to three typhoons in 1997, measured by a moored buoy in East China Sea. *Bond et al*. [2011] also described observations associated with the sea-air pCO_2 response to Typhoon Choi-wan (International designation 0914) in 2009 measured by the Kuroshio Extension Observatory (KEO) buoy. The former case was numerically studied by *Wada et al*. [2011a], while the latter has not been numerically investigated thus far.

[6] Unlike the three typhoons reported by *Nemoto et al*. [2009], Choi-wan underwent an extratropical transition at the location of the moored buoy. As a result, the horizontal distribution of surface winds was asymmetrical [*Bond et al*., 2011]. As will be shown later, the surface wind asymmetry leads to an added challenge for the numerical simulations. In particular, the asymmetric wind distribution should not be simply extracted from the six hourly atmospheric reanalysis with relatively coarse horizontal resolution (more than 20 km) but instead should be calculated by an atmosphere model with a relatively fine horizontal resolution (less than 10 km) that resolves the inner core of the typhoon. Alternatively, numerical simulations by a high-resolution coupled model can be used to investigate the effects of the asymmetric wind distribution of Choi-wan on the ocean response to Choi-wan.

[7] The purpose of this study is to analyze the interdisciplinary interactions between Choi-wan and the ocean using a sophisticated atmosphere-wave-ocean coupled model with a carbon equilibrium model (Figure 1). In particular, we focus on the following questions: (1) How does Choi-wan's wake occur at the KEO buoy? (2) What is the surface pCO_2^{sea} response to Choi-wan at the KEO buoy? (3) How does the oceanic response to Choi-wan affect the intensity and surface wind asymmetry of Choi-wan? (4) What roles does the initial oceanic field play in the simulations?

[8] It should be noted that as shown in Figure 1, the coupled model did not incorporate an atmospheric CO_2 model like *Sarrat et al*. [2007] or a biogeochemical scheme like *Huang and Imberger* [2010] and *Lévy et al*. [2012]. Therefore, this study focuses on simulations of the variation in pCO_2^{sea} without the effect of carbon fixation through plankton growth on the surface pCO_2^{sea}.

[9] This paper consists of five sections: Section 2 focuses on the experimental design, describing the physical and biogeochemical observations from the KEO-moored buoy, the numerical model and its specifications, and other oceanic and atmospheric data sets used in this study. Section 3 describes results of numerical experiments and their validation against the KEO mooring measurements and satellite sea-surface temperature (SST) fields. Section 3 also describes the results of sensitivity experiments for surface roughness-length schemes. Section 4 discusses the variation in pCO_2^{sea} by passage of Choi-wan and its relation to the oceanic initial field. In addition, section 4 discusses the effect of surface roughness lengths and associated surface winds on the atmospheric and oceanic ingredients observed at the KEO buoy. Finally, section 5 is devoted to concluding remarks.

2. Experimental Design

2.1. Observations at the KEO-Moored Buoy

[10] The KEO reference station is a highly instrumented moored buoy located at 32.3°N, 144.5°E, in the recirculation gyre south of the Kuroshio Extension [*Cronin et al*., 2008, 2013]. The measurement systems were reviewed in *Bond et al*. [2011]. In this study, we use data from the KEO mooring, including hourly meteorological data, hourly SST, and three hourly pCO_2 from a Moored Autonomous pCO_2 ($MAPCO_2$) system [*Bond et al*., 2011] for validation of the numerical simulation results. The $MAPCO_2$ uses a Licor-820 nondispersive infrared detector along with an in situ gas calibration to make surface seawater pCO_2 and marine boundary air CO_2 measurements that are traceable back to the standard of World Meteorological Organization (WMO). The Licor-820 is as a single path, dual wavelength infrared gas analyzer. The finalized data are available at the Carbon Dioxide Information Analysis Center (CDIAC; http://cdiac.ornl.gov/oceans).

2.2. Model

[11] A nonhydrostatic model (NHM) has been developed jointly by the Numerical Prediction Division and Meteorological Research Institute (MRI) of the Japan Meteorological Agency (JMA; hereafter JMANHM). The physical processes in the NHM include cloud physics expressed in an explicit three-ice bulk microphysics scheme based on the work of *Lin et al*. [1983], a resistance law assumed for air-sea momentum and enthalpy fluxes in the atmospheric surface boundary layer, exchange coefficients for air-sea momentum and enthalpy transfers over the sea based on *Louis et al*. [1982], a turbulent closure model in the atmospheric boundary layer formulated from the work of *Klemp and Wilhelmson* [1978] and *Deardorff* [1980], and an atmospheric radiation scheme based on *Sugi et al*. [1990]. The NHM used here is an older version of the current nonhydrostatic mesoscale model [e.g., *Saito*, 2012], but it is coupled with both a multilayer ocean model and a third-generation ocean-wave model [*Wada et al.*, 2010; *Wada*, 2012]. We used no cumulus parameterization in this study.

[12] The JMA third-generation ocean-wave model was coupled with the NHM to estimate changes in surface roughness lengths, drag coefficients, and enthalpy coefficients. The wave spectrum of the third-generation ocean-wave model consisted of 900 components, each associated with 1 of 25 frequencies and 1 of 36 directions. The frequency of the wave spectrum was divided logarithmically from 0.0375 to 0.3000 Hz. We assumed the ocean wave to be initially motionless. *Wada et al*. [2010] describe the detailed wave-ocean coupling procedure.

[13] We employed a reduced-gravity approximation and a hydrostatic approximation and assumed a Boussinesq fluid in the multilayer ocean model used here. The model had three layers (four levels). The uppermost layer represented the mixed layer, where the density was vertically uniform; the middle layer represented a seasonal thermocline, where the vertical temperature gradient was greatest; and the bottom layer was assumed to be undisturbed by entrainment. The four levels consisted of sea surface, the bases of the mixed layer, the seasonal thermocline, and the bottom (see section 2.4). Entrainment was calculated by using a multilimit entrainment formulation proposed by *Deardorff* [1983] and modified by *Wada et al*. [2009]. The model calculated water temperature and salinity at the surface and at the base of the mixed layer and calculated layer thickness and 2-D flows for all three layers. The model can simulate near-inertial currents behind a TC to some extent [*Wada*, 2002].

[14] In order to simulate the diurnal variation in SST precisely, we incorporated into the coupled model a scheme based on *Schiller and Godfrey* [2005]. We applied the short-wave radiation parameterization proposed by *Ohlmann and Siegel* [2000] to compute the absorption/penetration rate of short-wave radiation. A climatologically chlorophyll *a* created by *Kawai and Wada* [2011] was used as the initial and boundary conditions, and this study assumed that chlorophyll *a* was vertically uniform and constant during the integration. *Wada* [2010] describes the detailed procedure of the scheme.

[15] The atmosphere-ocean coupling procedure was as follows. Short-wavelength and long-wavelength radiation, sensible and latent heat fluxes, wind stresses, and precipitation were provided for every time step of the ocean model. Land and sea distributions extracted from GTOPO30 digital elevation data from the U.S. Geological Survey were provided from the atmosphere model to the ocean model only at the initial time in order to adjust the land and sea distributions between the atmosphere and ocean models. Ocean bottom topography was provided by ETOPO-5 data from the National Oceanic and Atmospheric Administration (NOAA) National Geophysical Data Center; these elevations are spaced at 5 min intervals of latitude and longitude. Conversely, SST calculated by the ocean model was provided for every time step of the ocean model.

[16] An oceanic carbon equilibrium scheme is based on the work of *Dickson et al*. [2007] and is coupled with the coupled atmosphere-wave-ocean model. The variation of pCO_2^{sea} was diagnostically calculated by the scheme under

the assumption that total alkalinity (ALK), total phosphate, and total silicate are constant. It should be noted that this assumption may not hold true during heavy rainfall of a typhoon. The evolution of dissolved inorganic carbon (DIC) was calculated by using the equation similar to the temperature and salinity equations in the multilayer ocean model, including advection, diffusion, vertical mixing, and air-sea fluxes due to evaporation and precipitation. However, the source minus sink term due to the biogeochemical pump was not included in the DIC equation (Figure 1). The representative depth for calculating the evolution of DIC was assumed to be 1 m. The sea-air CO_2 flux (F_{CO_2}) was calculated by using the short-term gas exchange-wind relationships derived by *Wanninkhof* [1992] in the following equation:

$$F_{CO_2} = ks\left(pCO_2^{sea} - pCO_2^{air}\right), \quad (1)$$

where k is the gas transfer velocity and s is the CO_2 solubility. The gas transfer velocity is assumed to be a function of second power of 10 m wind velocity [*Wanninkhof*, 1992]. More information on the carbon equilibrium scheme is described in the appendix of *Wada et al.* [2011a].

2.3. Best-Track Data

[17] We use the WMO Regional Specialized Meteorological Center (RSMC)-Tokyo best-track data recorded in the International Best track Archive for Climate Stewardship data set [*Knapp et al.*, 2010]. The RSMC-Tokyo is responsible for the distribution of information, advisories, and warning associated with TC in the Northwestern Pacific agreed by consensus at the WMO. The best-track data includes position, central pressure, and maximum wind speed every 6 h as usual. The history of RSMC-Tokyo best-track data set is described in the supplement of *Kamahori et al.* [2006]: A major source of TC intensity estimates is the *Dvorak* [1975] technique, which handles satellite image patterns.

[18] The position of Choi-wan at 1800 UTC on 19 September 2009 was 32.7°N, 145.1°E reported in the RSMC-Tokyo, the Hong Kong Observatory (HKO) and the China Meteorological Administration (CMA) and 32.3°N, 145.1°E reported in the Joint Typhoon Warming Center (JTWC). The best-track central pressure ranges 967 hPa in JTWC to 975 hPa in CMA at 1800 UTC on 19 September 2009. The best-track central pressure in RSMC-Tokyo and HKO is 970 hPa at the same time.

2.4. Design of Numerical Experiments

[19] The target typhoon in the present study is Typhoon Choi-wan (International designation 0914), which passed ~40 km to the southeast of the KEO mooring at ~1800 UTC on 19 September 2009. According to the RSMC-Tokyo best-track data, Choi-wan was generated when a tropical depression evolved into a TC around 15.4°N, 150.9°E at 1800 UTC on 12 September 2009. The typhoon moved initially west-northwestward but changed to a northwestward track as it rapidly intensified. From 1200 UTC on 15 September to 1800 UTC on 16 September, the minimum central pressure was 915 hPa and maximum wind speed was 105 knots (~54 m s^{-1}). At a location around 23.2°N, 138.9°E, the typhoon gradually slowed and changed to a north-northeastward track as it began to decay. The simulations performed here run for 96 h from 0000 UTC, 17 September 2009, through 0000 UTC, 21 September 2009, when the typhoon was mature and transitioning to an extratropical storm.

[20] JMANHM covers a 4000 × 4000 km domain with a horizontal grid spacing of 6 km. The horizontal resolution of 6 km is also applied to the third-generation ocean-wave model, the multilayer ocean model, and the oceanic carbon equilibrium scheme. JMANHM has 40 vertical levels with variable intervals from 40 m for the lowermost (near-surface) layer to 1180 m for the uppermost layer. JMANHM has maximum height approaching ~23 km. The time step of JMANHM was 15 s. The time step of the ocean model was 1.5 min and that of the third-generation ocean-wave model was 10 min.

[21] The initial depth of the oceanic mixed layer was determined from oceanic reanalysis data by defining the mixed layer as having a density difference from the surface of no more than 0.25 kg m^{-3} and a maximum depth of 200 m. The base of the thermocline was limited to 600 m, and water depth was limited to 2000 m. The oceanic reanalysis data were calculated using the MRI Ocean Variational Estimation (MOVE) system [*Usui et al.*, 2006].

[22] The initial time for all simulations was 0000 UTC on 17 September in 2009, when the typhoon entered its mature phase. Atmospheric initial and boundary conditions were derived from six hourly global objective analysis data from JMA with a grid spacing of 20 km. Oceanic initial conditions were derived from the MOVE system, forced with daily oceanic reanalyses. Because the integration time was 4 days, open oceanic boundaries were applied in series of numerical simulations. In order to investigate the impact of the horizontal resolution, two initialization fields were used: one with a large scale grid with a 0.5° horizontal spacing (experiment G6G5, see Table 1) and one with a regional scale grid with a 0.1° horizontal spacing (experiment G6G1). The initial conditions for DIC and ALK were derived from the empirical formulas based on in situ pCO_2^{sea} observations around 30°N, 137°E by research vessels and water temperature reanalyzed by MOVE [*Wada et al.*, 2011b]. Observed surface pCO_2^{sea} and pCO_2^{air} at the KEO buoy site were provided as the boundary conditions to calculate the sea-air CO_2 flux.

[23] Both JMANHM and coupled JMANHM-wave-ocean models were used to investigate the effect of the ocean on TC simulations from viewpoints of existence or nonexistence of sea-surface cooling induced by Choi-wan. Table 1 shows a list of numerical simulations to investigate the impact of sea-surface cooling and oceanic environmental field on the simulation of the typhoon. Experiments A6G5 and A6G1 used only the JMANHM model, while experiments C6G5 and C6G1 used the coupled JMANHM-wave-ocean model. Experiments A6G5 and C6G5 used the initial oceanic condition obtained from the oceanic reanalysis data set with a 0.5° horizontal spacing, while experiments A6G1 and C6G1 used a 0.1° horizontal spacing. All experiments used the same atmospheric initial and boundary conditions.

Table 1. Abbreviations of Numerical Experiments, Models, and Horizontal Resolutions of Model and MOVE

Experiments	Model	Horizontal Resolution of Model	Horizontal Resolution of MOVE
A6G5	JMANHM	6 km	0.5°
A6G1	JMANHM	6 km	0.1°
C6G5	JMANHM-wave-ocean coupled model	6 km	0.5°
C6G1	JMANHM-wave-ocean coupled model	6 km	0.1°

[24] The roughness-length scheme in experiments A6G5, A6G1, C6G5, and C6G1 was derived from an empirical formula of *Taylor and Yelland* [2001] (TY1) based on wave steepness. A change in surface roughness lengths leads to changes in drag and enthalpy air-sea exchange coefficients, indicating the changes in surface wind stresses and sensible and latent heat fluxes. The change of surface friction directly affects surface wind speed, and thus CO_2 flux (see equation (1)). In addition, the change in surface wind stresses can affect vertical turbulent mixing and ocean currents. In order to investigate the impact of surface roughness lengths on the interactions between Choi-wan and the ocean, sensitivity numerical experiments were performed in experiment C6G1 by using four different surface roughness schemes listed in Table 2, in addition to experiment TY1. These are described as follows. The roughness-length empirical formula of *Charnock* [1955] (CH1) was based on the constant value of the ratio of gravity acceleration multiplying surface roughness length to frictional velocity squared. *Janssen* [1991] proposed that the Charnock constant value varies depending on the ratio of wave-induced stress to wind stress (JA1), whereas *Smith et al*. [1992] proposed that the Charnock constant value varies depending on the ratio of frictional velocity to the wave age (SM1). The roughness-length scheme derived from an empirical formula of *Kondo* [1975] (KO1) was based on the dependency of 10 m wind speed on drag coefficients.

2.5. Satellite SST

[25] We use a daily satellite microwave SST data set on 17 and 20 September 2009 to validate the results of simulated SST field. The satellite data set (obtained from the site: http://www.ssmi.com/) includes two satellite SST data sets derived from two instruments: the Tropical Rainfall Measuring Mission (TRMM) Microwave Imager, and the Aqua/Advanced Microwave Scanning Radiometer for Earth observing system (AMSR-E) satellite radiometers. The merged satellite SST data set covers the global ocean with a 0.25° horizontal spacing.

Table 2. Abbreviations of Numerical Experiments and Surface Roughness-Length Schemes

Experiment	Roughness-Length Scheme
TY1 (=C6G1)	*Taylor and Yelland* [2001]
CH1	*Charnock* [1955]
JA1	*Janssen* [1991]
KO1	*Kondo* [1975]
SM1	*Smith et al*. [1992]

3. Results

3.1. Track and Intensity

[26] Figure 2 depicts simulated positions of Choi-wan for experiments A6G5, C6G5, A6G1, and C6G1 every 6 h and RSMC-Tokyo best-track positions of Choi-wan from 0000 UTC on 17 September. As can be seen in Figure 2, the simulated positions differ little among the four experiments, indicating that Choi-wan's track simulation is little affected by sea-surface cooling induced by Choi-wan and a difference of horizontal resolution of MOVE data between two initial environmental fields of the ocean (Figure 2a). The track simulation agreed well with the observed track (Figure 2a), although the simulated translation speed was slower, particularly at 1800 UTC on 19 September (Figure 2b), when the typhoon came close to the KEO-moored buoy. Indeed, the simulated-typhoon translation speed was $\sim$10.5 m s^{-1} in experiment C6G1, and the best-track translation speed was $\sim$13.8 m s^{-1}, $\sim$3 m s^{-1} faster than the simulation at 1800 UTC on 19 September (Figure 2b).

[27] Figure 3 depicts the time series of Choi-wan's simulated central pressures for experiments A6G5, C6G5, A6G1, and C6G1 and RSMC-Tokyo best-track central pressure every 6 h. Although the best-track central pressure rises during the integration due to the mature-to-decaying phases, the results of simulated central pressures in all experiments (Table 1) show intensification at an early integration due to a spin-up process. After 0600 UTC on 18 September, simulated central pressures begin to rise. The tendency of simulated central pressure is comparable to that of the best-track central pressure.

[28] In Figure 3, we find that both sea-surface cooling induced by Choi-wan and a difference between two oceanic initial fields affect the central-pressure simulations. The impact of sea-surface cooling on the central-pressure simulations is more remarkable than that of the difference between two initial environmental fields of the ocean, which is consistent with the conclusion of *Wada and Usui* [2010]. This suggests that the increase in simulated central pressures due to sea-surface cooling is mainly caused by reduction in turbulent heat fluxes within the inner core of simulated Choi-wan (not shown), which is consistent with *Zhu et al*. [2004].

3.2. Validation of Numerical Results Using KEO Buoy Observations

3.2.1. Atmospheric Components

[29] Because the coupled model used in this study does not incorporate an atmosphere CO_2 model (Figure 1) and thus cannot compute the variation in pCO_2^{air}, we validated the variation in computed sea-level pressure and air

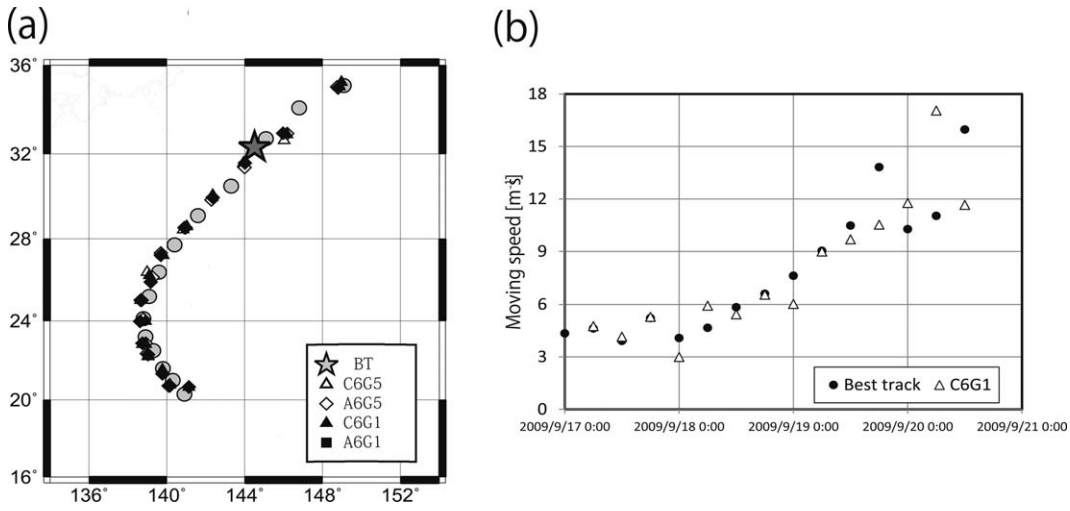

Figure 2. (a) Simulated positions for experiments A6G5, C6G5, A6G1, and C6G1 every 6 h and RSMC-Tokyo best-track positions of Choi-wan every 6 h from 0000 UTC on 17 September. (b) Time series plot of translation speeds of best-track and simulated Choi-wan (C6G1) every 6 h.

temperature at the buoy station using the moored buoy observations. However, before using these data for validating the numerical simulations, it is important to determine whether the large variation in ΔpCO_2 ($pCO_2^{sea} - pCO_2^{air}$) observed during the typhoon passage [*Bond et al.*, 2011] is associated with the sea component, air component, or a combination of the two.

[30] Figure 4 depicts the time series plot of pCO_2^{air} measured by the KEO mooring. The concentration of pCO_2^{air} was calculated from the fugacity of CO_2 (fCO_2) determined by mole fraction of CO_2 (xCO_2) measurement. The concentration of pCO_2^{air} was 367.3 μatm at the initial time of the integration, at 0000 UTC on 17 September. The concentration of pCO_2^{air} gradually decreased and then at 57 h, 0900 UTC on 19 September, began to rapidly decrease. The concentration of pCO_2^{air} reached the minimum value of 348.3 μatm at 66 h, 1800 UTC, and then began to increase after the passage of Choi-wan. The concentration of pCO_2^{air} reached the minimum when observed sea-level pressure was lowest at the KEO-moored buoy (Figure 5).

[31] Observed air temperature became low when the sea-level pressure was relatively low during the passage of Choi-wan. After the passage, observed air temperature increased (Figure 5). The numerical experiment in experiment C6G1 reproduced rapid variation in sea-level pressure at the moored buoy reasonably well, although the peak appeared 3 h later than observed. Simulated air temperature tended to be lower from 36 to 48 h than observed due to seasonal rain front that was not observed. Simulated air temperature tended to be higher from 54 to 69 h than observed due to the slower approaching Choi-wan in the simulation. After 72 h, simulated air temperature was lower

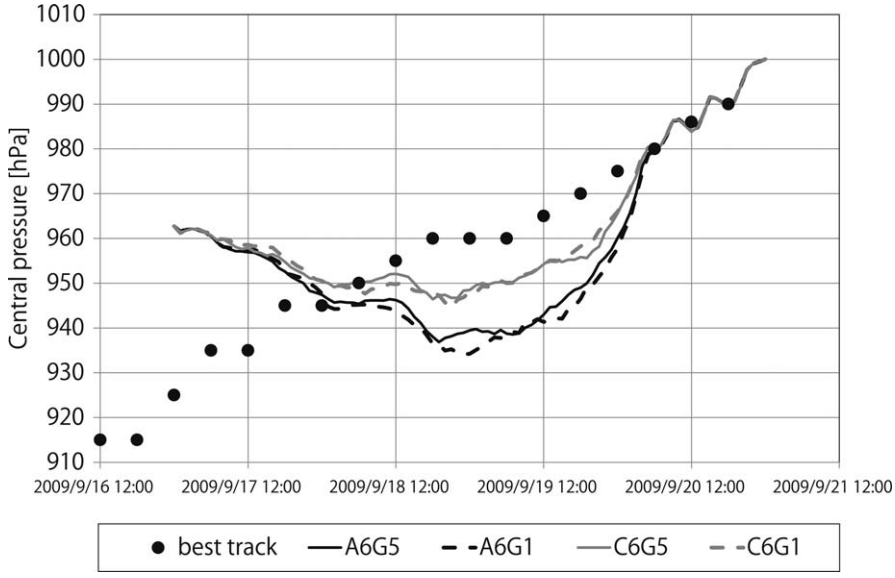

Figure 3. Time series of Choi-wan's simulated central pressures for experiments A6G5, C6G5, A6G1, and C6G1 and RSMC-Tokyo best-track central pressure every 6 h.

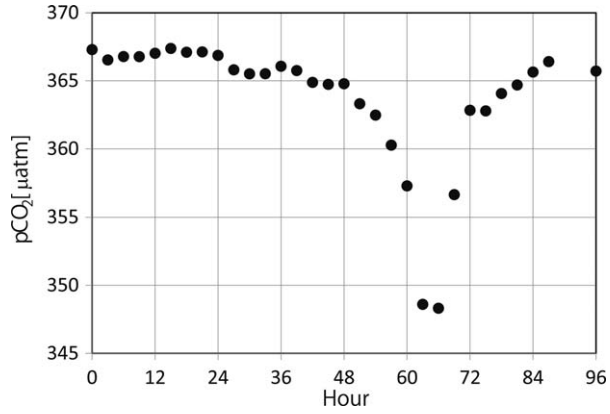

Figure 4. Time series of pCO_2^{air} observed at the moored buoy. The *x* axis indicates the integration time.

than observed. It should be noted that while the simulated central pressures tended to be low in all experiments compared with the best-track central pressure (Figure 3), the simulated sea-level pressure at the KEO grid point was comparable with the time-shifted KEO observations (Figure 5). The inconsistency between the best-track TC intensity estimate and observations may be related to the limit of the *Dvorak* [1975] technique. Because pCO_2^{air} at the KEO-moored buoy was sensitive to in situ sea-level pressure, the relatively good simulation of sea-level pressure at the KEO site suggests that the model should be able to investigate the occurrence of rapid variation in ΔpCO_2.

3.2.2. Physical and Biochemical Oceanic Response to Choi-wan

[32] *Bond et al*. [2011] reported in their Figure 4 that ΔpCO_2 rapidly increased more than 50 μatm at the KEO-moored buoy during the passage of Choi-wan. Nearly 40% of ΔpCO_2 was explained by rapidly falling pCO_2^{air} during the passage (Figure 4). In other words, nearly 60% of ΔpCO_2 must be explained by a rapid increase in pCO_2^{sea}. Here we address the effect of Choi-wan-induced physical pump on the increase in surface ocean pCO_2^{sea} using the results of numerical simulation in experiment C6G1 and observations measured by the KEO mooring.

[33] As a first step, the initial vertical profiles of water temperature and salinity reanalyzed by MOVE were compared with the profiles observed at the KEO-moored buoy (Figure 6). Water temperature observed at the KEO-moored buoy was ∼0.8°C higher, and observed salinity was ∼0.15 psu lower at the mixed-layer base than the initial water temperature and salinity reanalyzed by MOVE (Figure 6). Errors of water temperature and salinity were relatively large at the seasonal thermocline. However, high mixed-layer temperature and low mixed-layer salinity observed at the KEO-moored buoy were reasonably reproduced by MOVE.

[34] Figure 7 displays the horizontal distributions of satellite SST, simulated SST, pCO_2^{sea}, and sea-surface salinity (SSS) in experiment C6G1 at the initial time of integration on 17 September. Initial pCO_2^{sea} was diagnostically calculated by the carbon equilibrium scheme incorporated into the atmosphere-wave-ocean coupled model (Figure 1). Horizontal gradients of SST were reasonably reproduced by MOVE around the Kuroshio Extension region. However, MOVE SST was relatively high around 36°N, 147°E, east of a trough of cold water, whereas satellite SST was relatively high around 34°N, 142°E, west of the trough. The horizontal distribution of pCO_2^{sea} at the initial time was similar to that of MOVE SST, indicating that an error of pCO_2^{sea} was attributed to that of the MOVE SST.

[35] Time series plots of SST, pCO_2^{sea}, pCO_2^{sea} normalized to a temperature of 29°C, and SSS measured by the KEO mooring were compared with those in experiment C6G1 (Figure 8). It should be noted that during the passage of Choi-wan, the $MAPCO_2$ diagnostics show pressure abnormalities that could impact the pCO_2^{sea} measurements. However, those abnormalities can be expected to occur during typhoon conditions, and we assume here that those measurements are of acceptable quality. pCO_2^{sea} normalized to a temperature of 29°C was computed for both observed and simulated SST and pCO_2^{sea} (Figure 8b) in order to extract the variations in pCO_2^{sea} independent of water temperature. SST measured by the KEO mooring cools by ∼1°C from 1800 UTC on 19 September (66 h) to 1200 UTC on 20 September (84 h). On the other hand, SST in experiment C6G1 is cooled by ∼2.5°C during the same period at a grid point corresponding to the KEO-moored buoy.

[36] After the passage of Choi-wan, we find that the observed pCO_2^{sea} rises ∼10 μatm (Figure 8b) and observed SSS (Figure 8c) rises by ∼0.3 psu from the initial value. In contrast, simulated SSS rapidly decreases after the passage of Choi-wan, resulting in the rapid decrease in pCO_2^{sea}. This indicates that the numerical simulations poorly captured the local variation in observed SST, pCO_2^{sea}, and SSS after the passage of the typhoon. In addition, we investigated the evolution of the normalized pCO_2^{sea} at the KEO-moored buoy (Figure 8b). The normalized pCO_2^{sea} slightly decreased after the passage of the typhoon, which was not consistent with the result of *Wada et al*. [2011a].

[37] Figure 9 displays the horizontal distribution of satellite SST on 20 September and the corresponding simulated SST, surface ocean pCO_2^{sea}, and SSS (at 84 h). Satellite SST partly captures sea-surface cooling induced by Choi-wan around 29°N, 143°E. Sea-surface cooling also existed around 34°N, 145°E north of the KEO-moored buoy. The simulated Choi-wan passed by on the right (east) side of the

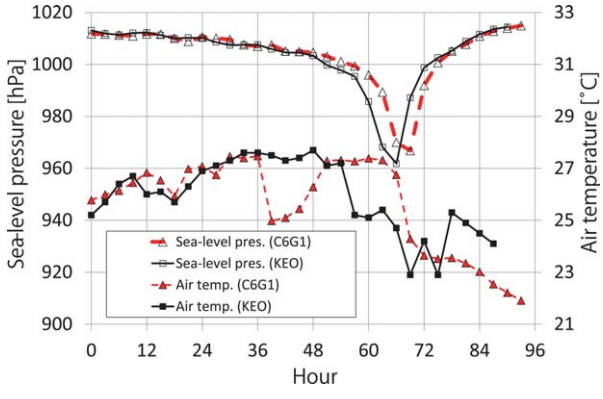

Figure 5. Time series of air temperature and sea-level pressure observed at the moored buoy and simulated in experiment C6G1 at the grid (32.3°N, 144.5°E).

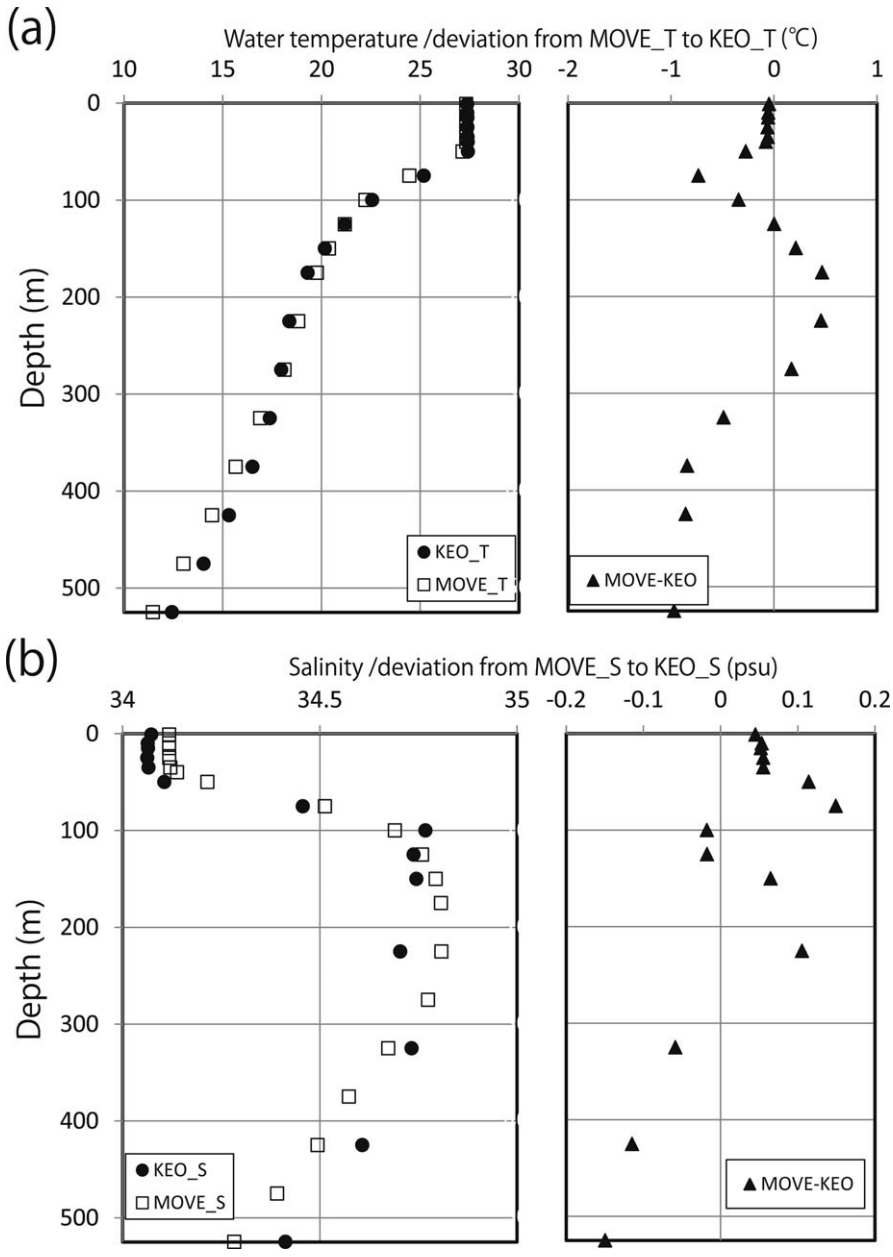

Figure 6. (left) Vertical profiles of (a) observed and reanalyzed water temperature and (b) salinity at the location of the moored buoy and (right) deviations between observed and reanalyzed (a) water temperature and (b) salinity. Reanalysis was conducted by MOVE.

KEO buoy. The simulated central pressure was lower than the best-track central pressure (Figure 3), although that was close to the observed central pressure at the buoy (Figure 5). Near the KEO buoy, the $\sim$3 m s^{-1} slower translation (Figure 2b) resulted in more unrealistic simulations of the near-inertial currents, horizontal advection, and turbulent mixing behind Choi-wan, resulting in excessive sea-surface cooling relative to the KEO and satellite observations.

[38] Low SSS and resultant low surface ocean pCO_2^{sea} were simulated in the region of KEO (Figures 9c and 9d). The area of low SSS and low pCO_2^{sea} extended west to northwest from the buoy, associated with the oceanic response to seasonal rain front that caused heavy rainfall in experiment C6G1 (not shown). In fact, north of the buoy, SST on the left (west) side of the track decreased sharply according to the satellite SST (Figure 9a), and the initial SST reanalyzed by MOVE was relatively low (Figure 9b). This suggests that the numerical simulation at the KEO site depends upon the change of the background seasonal structure of the ocean.

[39] Figure 10 displays the horizontal distribution of the difference in SST between the initial time and 84 h in satellite SST (Figure 10a) and that in simulated SST (Figure 10b) in experiment C6G1. South of 30°N around 140°E–144°E the cool wake observed by satellite SST was on the right side of the moving typhoon (Figures 9a and 10a), whereas sea-surface cooling induced by Choi-wan was primarily simulated along the track (Figure 10b). Around the

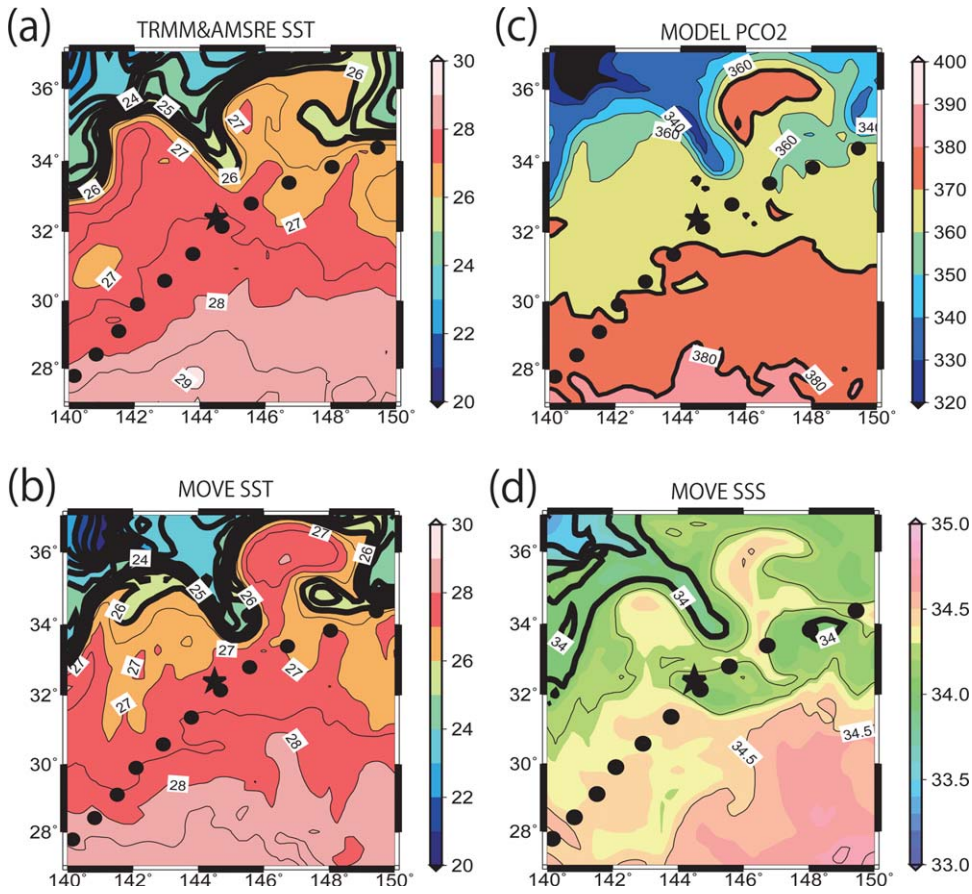

Figure 7. Horizontal distributions of (a) daily TRMM and AMSR-E merged SST on 17 September, (b) initial SST, (c) initial pCO_2^{sea}, and (d) initial SSS at 0000 UTC on 17 September. Black circles indicate simulated Choi-wan's positions in experiment C6G1 every 3 h. A black star indicates the location of the KEO-moored buoy.

KEO buoy, satellite SST tended to be relatively low north to west of the buoy, where it zonally extended along 32°N–34°N. The zonal negative deviation of SST shifted northward in experiment C6G1, corresponding to the location of simulated stagnant seasonal rain front. It should be noted that the simulated SST is a snapshot every time step of the model, while satellite SST is a daily product and cannot cover the entire computational domain at a given time step.

[40] Figures 11a and 11b display the horizontal distributions of DIC at the initial time (Figure 11a) and 84 h integration time (Figure 11b). At the initial time of integration, DIC showed a distribution that became high with increasing latitude, corresponding to the SST distribution (Figure 7b). At 84 h, DIC alternatively increased and decreased along the simulated track of Choi-wan due to near-inertial currents and vertical turbulent mixing. The area of relatively high DIC corresponded to that of relatively high SSS and SST. The near-inertial pumping [*Price*, 1983] induced by near-inertial currents and vertical turbulent mixing led to relatively high DIC and SSS, resulting in high pCO_2^{sea} in spite of relatively low SST. Near-inertial pumping on a weather-forecasting time scale differs in spatial and temporal scales from the Peruvian upwelling on seasonal to interannual time scale [*Ishii et al*., 2004], although the physics are similar to each other. The KEO-moored buoy was in a small region of low DIC water, surrounded by high DIC water (exceeding 2030 μmol kg^{-1} at 84h). It may be presumed that the increase in observed surface pCO_2^{sea} after the passage of Choi-wan (Figure 8b) was influenced by increasing DIC. However, simulated DIC at the KEO buoy became rather small. Unrealistic low DIC water at the buoy accompanied by low SSS resulting in low pCO_2^{sea} water may be caused by errors in the MOVE initial oceanic field, initial conditions in the multilayer model and atmospheric forcing due to errors in simulated Choi-wan's track and simulated stagnant seasonal rain front.

[41] Thus, it is not appropriate to compare the rapid variation in ΔpCO_2 observed by the moored buoy directly to the numerical simulation at the location of the moored buoy. Instead, considering the 3 h delay of the track of the simulated typhoon and alternative pattern of simulated DIC along the track, we compared the moored buoy observations with a grid point south of the KEO-moored buoy (31.9°N, 144°E) in the simulated-typhoon reference frame, where pCO_2^{sea} (Figure 10c), SSS (Figure 10d), and DIC (Figure 11b) were higher than those in the surroundings as the simulated typhoon passed by. Figure 12a shows the time series of DIC analyzed by observed SST, SSS, and pCO_2^{sea} using the oceanic carbon equilibrium scheme alone (hereafter analyzed DIC) and simulated DIC at the KEO buoy and south of the KEO buoy. Even though the initial

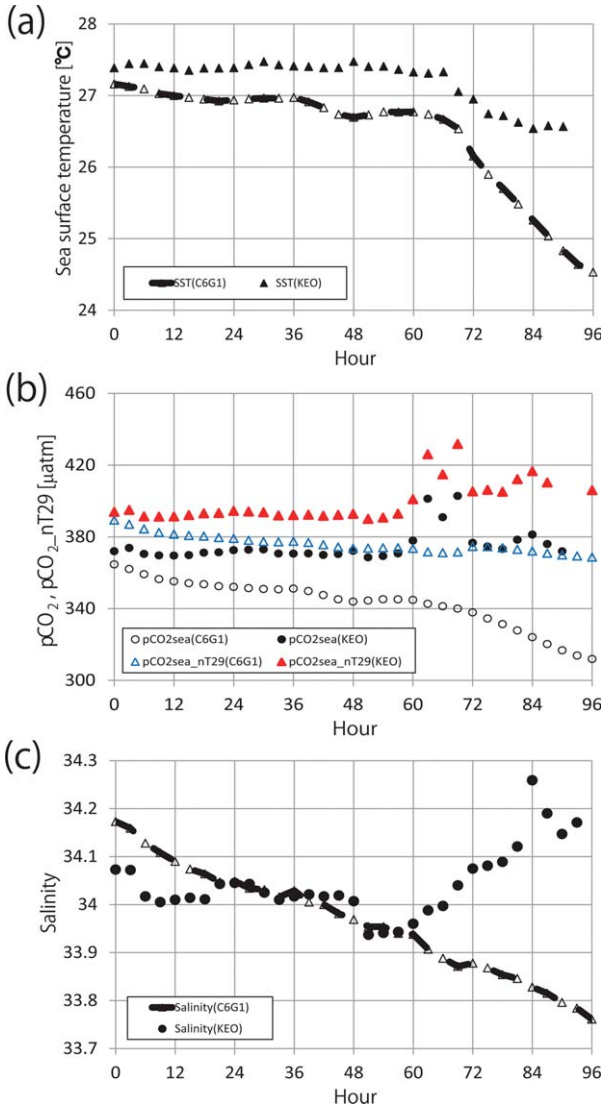

Figure 8. (a) Time series of SST and surface pCO_2^{sea} observed at the moored buoy and simulated in experiment C6G1 at the grid (32.3°N, 144.5°E). (b) Same as Figure 7a except for the time series of pCO_2^{sea} and normalized pCO_2^{sea} to a temperature of 29°C. (c) Same as Figure 7a except for the time series of SSS.

values differed between simulated and analyzed DIC at the KEO buoy, the simulation could not reproduce both the temporal variation in DIC during the passage of Choi-wan and the increase in DIC exceeding 5 µmol kg^{-1} after the passage. Figure 12b shows the time series of sea-air CO_2 flux at the KEO buoy and south of the buoy. A peak of sea-air CO_2 flux was found at the KEO buoy, whereas there were bimodal peaks south of the buoy. The bimodal pattern was similar to that of analyzed DIC and observed pCO_2^{sea} at the KEO buoy, but it should be noted that sea-air CO_2 flux plays a role in decreasing DIC.

[42] The initial vertical profiles of water temperature and salinity in the MOVE reanalysis south of buoy are compared with the profiles at the KEO-moored buoy (Figure 13). We can clearly find that the mixed-layer salinity south of the KEO buoy is higher than that at the KEO buoy, and water temperature south of the KEO buoy is lower than that at the KEO buoy particularly below the mixed-layer depth.

[43] South of the KEO-moored buoy, the results of numerical simulations in experiment C6G1 indicate the existence of high pCO_2^{sea} and high SST water around 31.9°N, 144°E at 84 h, corresponding to the location near the position of simulated typhoon at 66 h (Figure 9). The time series plot of simulated sea-level pressure around 31.9°N, 144°E in experiment C6G1 agrees well with that measured by the KEO mooring (Figure 14a), although air temperature still tends to be high before and during the passage of Choi-wan. High simulated air temperature around 31.9°N, 144°E indicates that the area is not affected by simulated seasonal rain front and accompanied heavy rainfall. Therefore, the error of the simulation of seasonal rain front may affect the error of simulated air temperature at the KEO buoy during the passage of Choi-wan.

[44] Simulated SST in experiment C6G1 near 31.9°N, 144°E at 84 h cools by ~2.5°C from the initial time (Figure 14b), corresponding to that simulated at the KEO-moored buoy. The time series of surface pCO_2^{sea} and SSS around 31.9°N, 144°E show increases in pCO_2^{sea} (Figure 14c) before and during the passage of the typhoon and those in SSS (Figure 14d) during the entire integration time. The variation in simulated pCO_2^{sea} normalized to a temperature of 29°C agrees roughly with the observed normalized pCO_2^{sea} ; therefore, both observed and simulated normalized surface pCO_2^{sea} increased during the passage of the typhoon. The maximum simulated pCO_2^{sea} was 377.1 µatm at 69 h, which was ~9.6 µatm higher than the initial pCO_2^{sea} (Figure 14c), corresponding to only about 20% of ΔpCO_2 and one third of the increase in surface pCO_2^{sea} observed at the KEO buoy. These results suggest that relatively small sea-surface cooling, high salinity, and high DIC after the passage of Choi-wan can contribute to the increase in ΔpCO_2. However, the coupled model could not simulate the rapid variations in pCO_2^{sea} that occurred on timescales less than a half day during and after the passage of the typhoon.

3.2.3. Surface Roughness Length

[45] As described in the previous section, simulated surface pCO_2^{sea} can be determined from SST, SSS, DIC, and ALK by the oceanic carbon equilibrium scheme incorporated into the coupled model (Figure 1). In addition, the evolution of SST, SSS, and DIC is calculated through the numerical integration of the coupled model under given initial atmospheric and oceanic conditions. Previous studies reported that the typhoon-induced sea-surface cooling is caused primarily by upwelling and vertical turbulent mixing [e.g., *Wada et al*., 2009], and the impact of turbulent heat fluxes on the sea-surface cooling is relatively small [e.g., *Price*, 1981]. Surface wind velocity and air-sea exchange coefficients for air-sea momentum and enthalpy transports play an essential role in determining wind stresses and turbulent heat fluxes, resulting in upwelling, near-inertial currents, and vertical turbulent mixing. In addition, surface wind velocity and gas transfer velocity influence sea-air CO_2 fluxes, as is shown is equation (1). Recent studies indicated that the exchange coefficient for air-sea momentum levels off at wind speeds over 30–40 m s^{-1} [e.g., *Powell et al*., 2003]. High surface winds derived

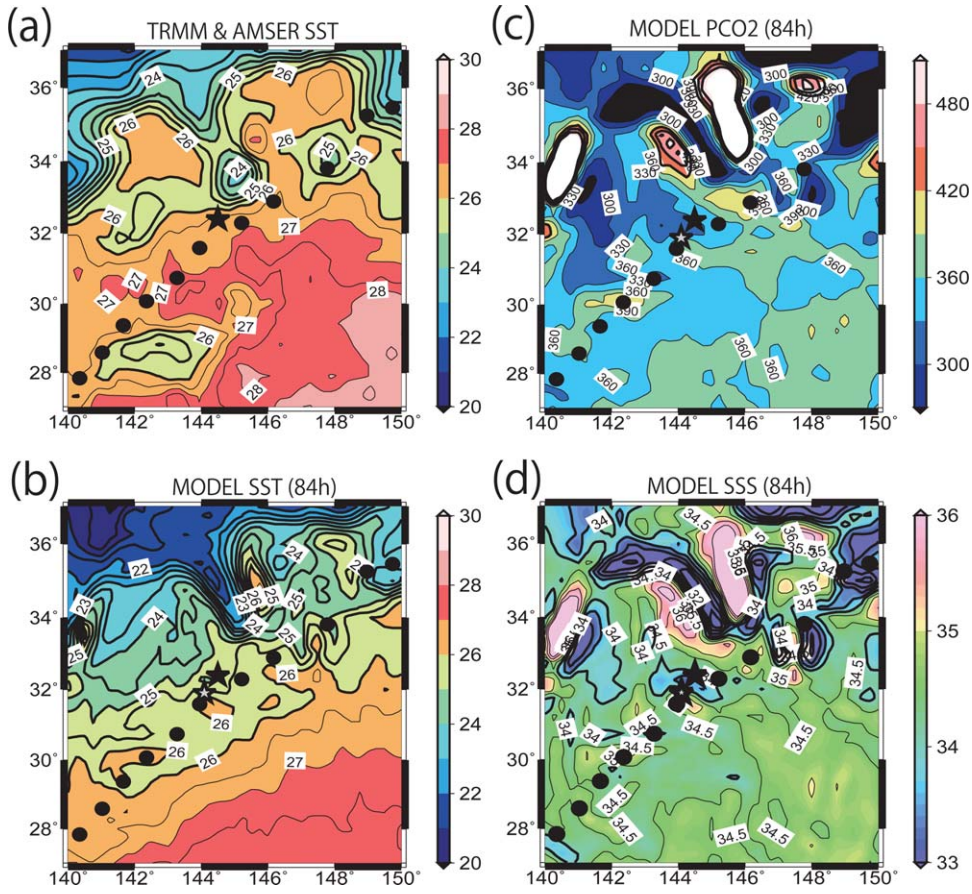

Figure 9. Same as Figure 6 except for (a) on 20 September and (b)–(d) at 84 h. A gray star indicates the location around 31.9°N, 144°E.

from relatively low exchange coefficients for air-sea momentum help increase in CO_2 effluxes.

[46] Air-sea exchange coefficients are calculated in JMANHM and the coupled model using surface roughness lengths and Monin-Obukhov similarity theory based on *Louis et al*. [1982]. Surface wind velocity (10 m wind velocity) is calculated in both models based on the Monin-Obukhov similarity theory. Consequently, surface roughness lengths are closely related to surface winds. It is of great importance to know whether errors of simulated sea-surface cooling and pCO_2^{sea} induced by Choi-wan are caused by errors in the parameterization of physical processes used by the model and in resultant surface winds. Therefore, this section addresses the impact of surface roughness lengths varied by ocean waves on the interactions between Choi-wan and the ocean.

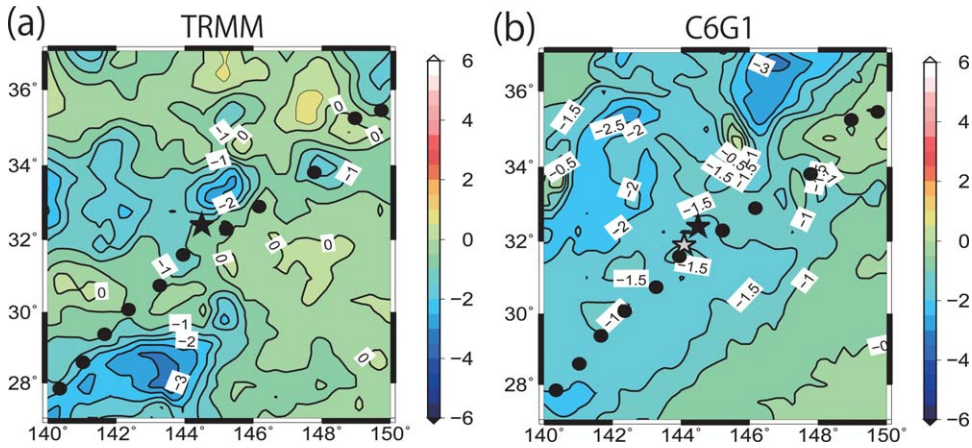

Figure 10. Horizontal distribution of a difference in (a) satellite SST (°C) and (b) simulated SST (°C) in experiment C6G1 between the initial time and 84 h.

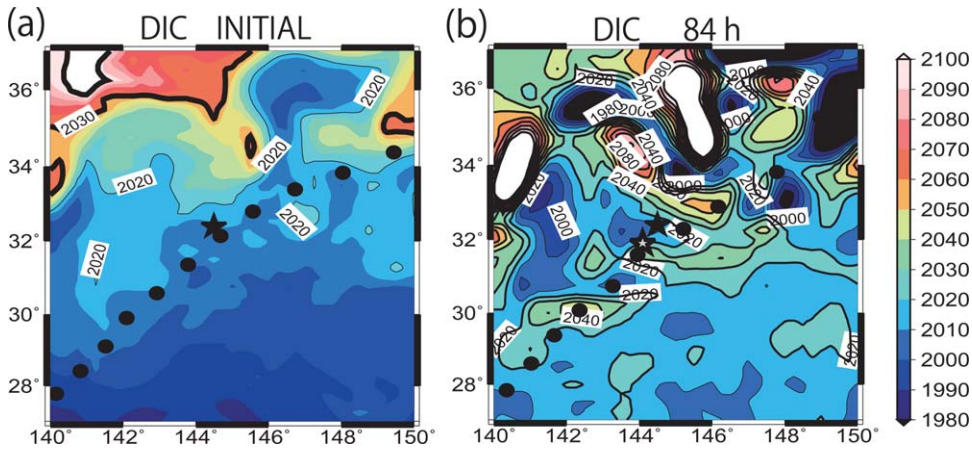

Figure 11. Horizontal distributions of DIC (μmol kg^{-1}) at (a) the initial time and (b) 84 h. Black circles indicate simulated Choi-wan's positions in experiment C6G1 every 3 h. A star indicates the location of the KEO-moored buoy.

[47] Figures 15a and 15b depict the relation of 10 m wind speeds to surface roughness lengths and drag coefficients at 72 h in experiments TY1 (=C6G1), CH1, JA1, KO1, and SM1 (Table 2). Surface roughness lengths and drag coefficients monotonically increased as 10 m wind speeds increased in experiments CH1, JA1, SM1, and KO1 but not in experiment TY1. The values exponentially increased in experiment SM1 and were relatively high compared with those in experiments CH1, JA1, and KO1. This indicates that surface friction in experiment SM1 was strongest of all experiments. In experiment TY1, the values of surface roughness lengths and drag coefficients sharply decreased with increasing wind speed for 10 m wind speeds in excess of 25 m s^{-1}. This sharp decrease in drag coefficients is consistent with the observational results of *Powell et al*. [2003] and indicates that wave steepness plays a crucial role in lowering surface roughness lengths and drag coefficients when surface winds are high. Simulated drag coefficients in experiment TY1 and enthalpy coefficients in all experiments (not shown) are reasonable with previous studies reported in the seventh WMO International Workshop on Tropical Cyclones (http://www.wmo.int/pages/prog/arep/wwrp/tmr/otherfileformats/documents/SF1b-PBlacknJHawkins.pdf).

[48] The difference among surface roughness-length schemes directly affected central pressures simulated by the coupled model (Figure 15c) but had little effect on the track simulations (Figure 16). A difference in simulated central pressures among the five experiments began to appear at 45 h (Figure 15c). High values of drag coefficients led to high simulated central pressures, particularly in experiments TY1 and SM1 after 66 h. However, simulated central pressure in experiment SM1 was low during the intensification phase due to intensification of frictional inflow. In contrast, simulated central pressures tended to be low in experiments CH1, JA1, and KO1, which had lower drag coefficients.

[49] By 19 September 2009, Choi-wan underwent extratropical transition and as a consequence the horizontal distribution of wind speeds became asymmetric, with higher wind speeds in the southeastern quadrants of the typhoon [see *Bond et al*., 2011, Figure 2]. The simulated surface wind speed in experiment TY1 had a wavenumber-1 pattern with high speeds only in the western quadrant (Figure 16a), whereas that in experiment SM1, with higher wind speeds in the southwestern quadrant, had a different asymmetry from that in experiment TY1 (Figure 16b). In fact, the asymmetric surface wind pattern in experiment SM1 is similar to that reported by *Bond et al*. [2011] even though high wind speeds appear in the southeastern quadrant. This study shows that a difference of surface roughness-length

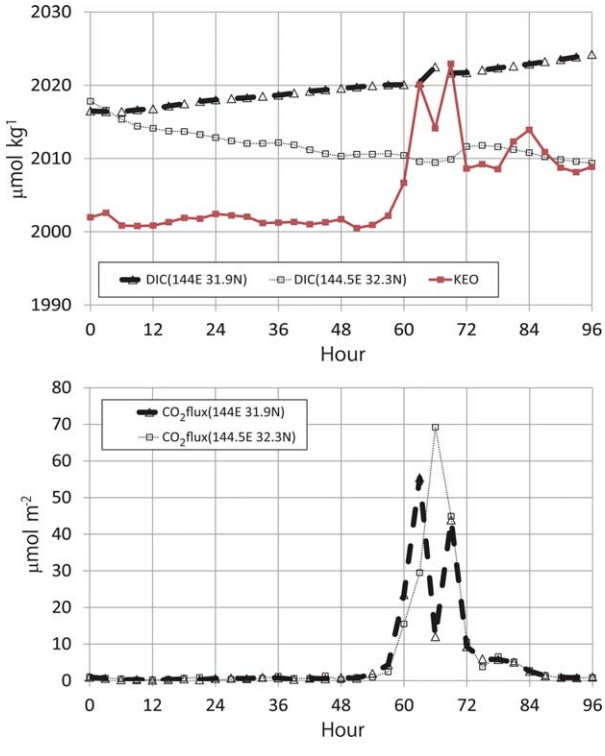

Figure 12. Time series of (a) DIC and (b) sea-air CO_2 flux at the KEO buoy (32.3°N, 144.5°E) and at 31.9°N, 144°E. The red line in (a) indicates the time series of DIC analyzed by observed SST, SSS, and pCO_2^{sea} using the carbon equilibrium scheme alone.

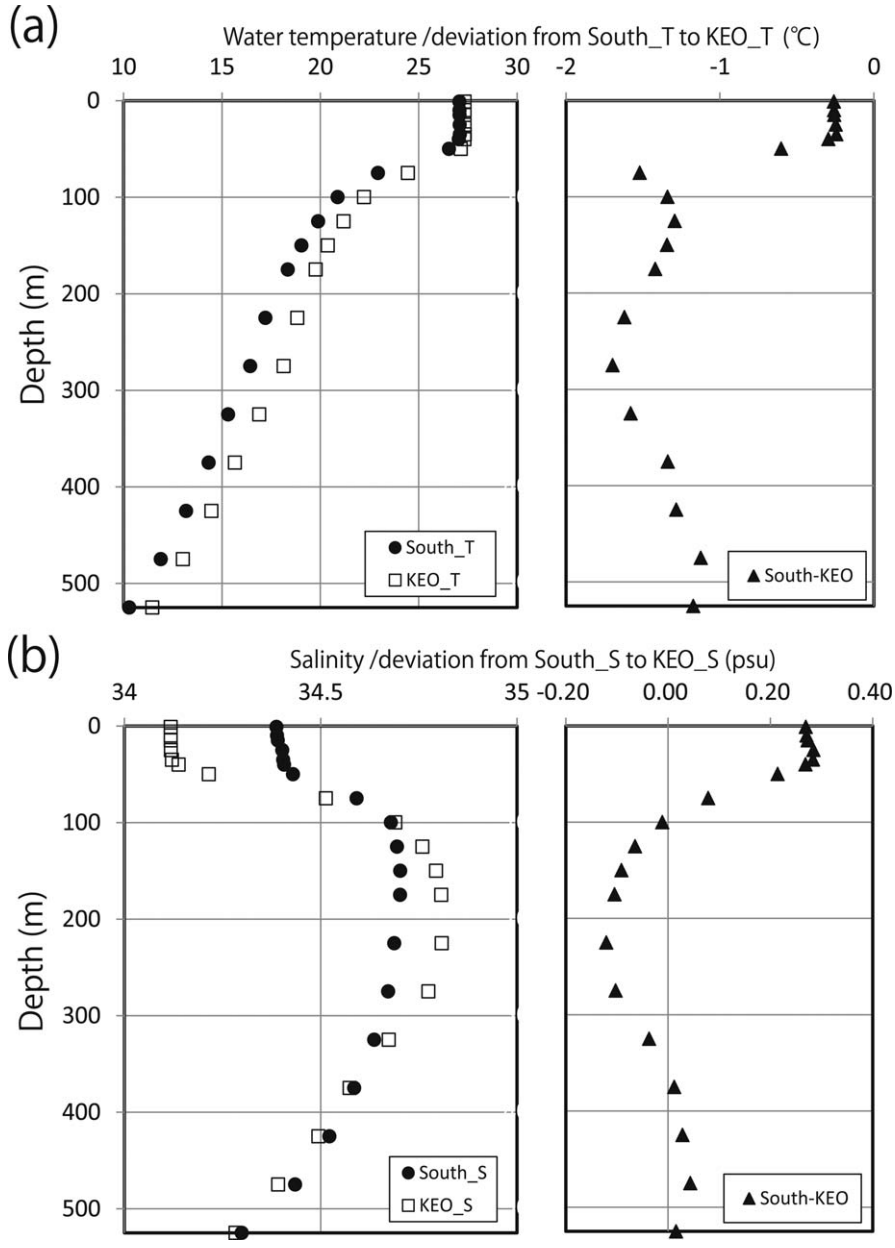

Figure 13. Same as Figure 5 except for the comparison of the vertical profiles at the KEO buoy with those at 31.9°N, 144°E.

scheme could change the asymmetry of surface wind pattern as well as the simulated central pressure.

[50] The time series plots of simulated sea-level pressure near 31.9°N, 144°E in the five experiments are shown in Figure 17a. A difference in simulated sea-level pressure defined by the deviation from the maximum to the minimum value among the five schemes was ∼9.1 hPa at 66 h. At 66 h, the difference in simulated air temperature, SST, and SSS was ∼0.78°C, ∼0.07°C, and ∼0.004 psu, respectively. The differences indicate that the impact of the different surface roughness-length schemes on SST and SSS seems to be much smaller than on sea-level pressure and air temperature, although the impact on SSS becomes large after the passage of Choi-wan (Figure 17e).

[51] Sensitivity numerical experiments indicate that a difference in DIC, pCO_2^{sea}, and sea-air CO_2 flux between the five schemes was nearly 2.4 μmol kg^{-1}, 1.0 μatm, and 48.4 μmol m^{-2}, respectively. The difference of surface roughness lengths had a large impact on sea-air CO_2 flux, relatively large effect on pCO_2^{sea} but a small impact on DIC. Rather, the difference in pCO_2^{sea} between the schemes was a little smaller after the passage of the typhoon than that of pCO_2^{sea} between the location of the KEO-moored buoy and around 31.9°N, 144°E, caused by the difference of oceanic field. Nevertheless, this study presented here is the first work that shows changes in surface roughness lengths that affect the variation in pCO_2^{sea} to some extent during and after the passage of the typhoon.

[52] It should be noted that the effect on pCO_2^{sea} is relatively small compared with that on sea-air CO_2 flux. This is because the variation in pCO_2^{sea} is caused by both wind and vertical mixing effects during and after the storm [*Lévy et*

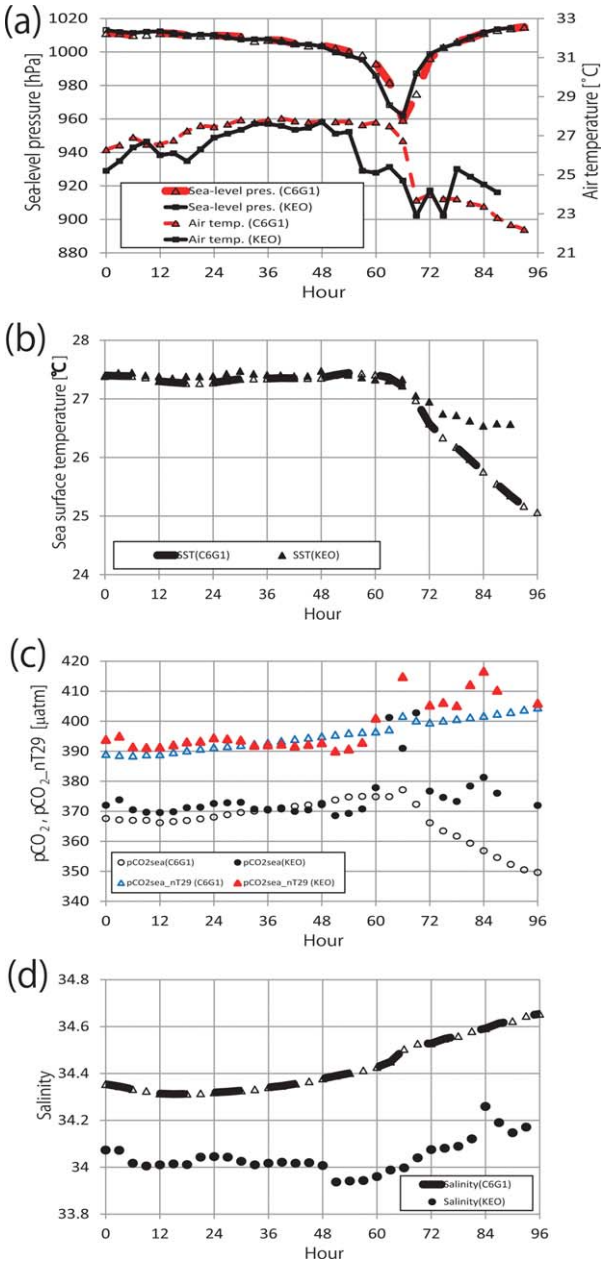

Figure 14. Time series plots of observed and modeled (a) air temperature and sea-level pressure, (b) SST, (c) surface pCO_2^{sea} and normalized pCO_2^{sea} to a temperature of 29°C, and (d) SSS. The location of model ingredients is 31.9°N, 144°E.

al., 2012], whereas sea-air CO_2 flux during the storm is determined only by the wind effect.

4. Discussion

4.1. Oceanic Initial Conditions and the Oceanic Response to Choi-wan

[53] The initial value of pCO_2^{sea} is calculated diagnostically using SST, SSS, DIC, and ALK in this study. The initial values of DIC and ALK are determined from water temperature, based on empirical formulas proposed by *Wada et al*. [2011b] formulated from historical research vessel observations around 30°N, 137°E. Therefore, an initial SST error can lead to that of simulated pCO_2^{sea}. However, in addition to SST, subsurface water temperature, and salinity can also affect the simulation of pCO_2^{sea} through oceanic physical processes such as horizontal and vertical advection (including upwelling and near-inertial pumping) and vertical turbulent mixing. Compared with the initial water temperature and salinity at the buoy, SSS is ~0.3 high around 31.9°N, 144°E (Figure 13). It should be noted that the initial vertical profile of salinity in the multilayer ocean model could not capture high-salinity water in the thermocline at the buoy site as it has only three layers. SSS simulations throughout the entire integration are strongly influenced by the initial vertical profile of salinity.

[54] As shown in Figure 1, this study neglects the effect of biogeochemical pump on DIC because oceanic water of the Kuroshio Extension region is oligotrophic, and the integration time is only 4 days [*Huang and Imberger*, 2010]. In addition, we have not sufficiently investigated the impact of atmospheric aerosols on DIC and pCO_2^{sea} as a source

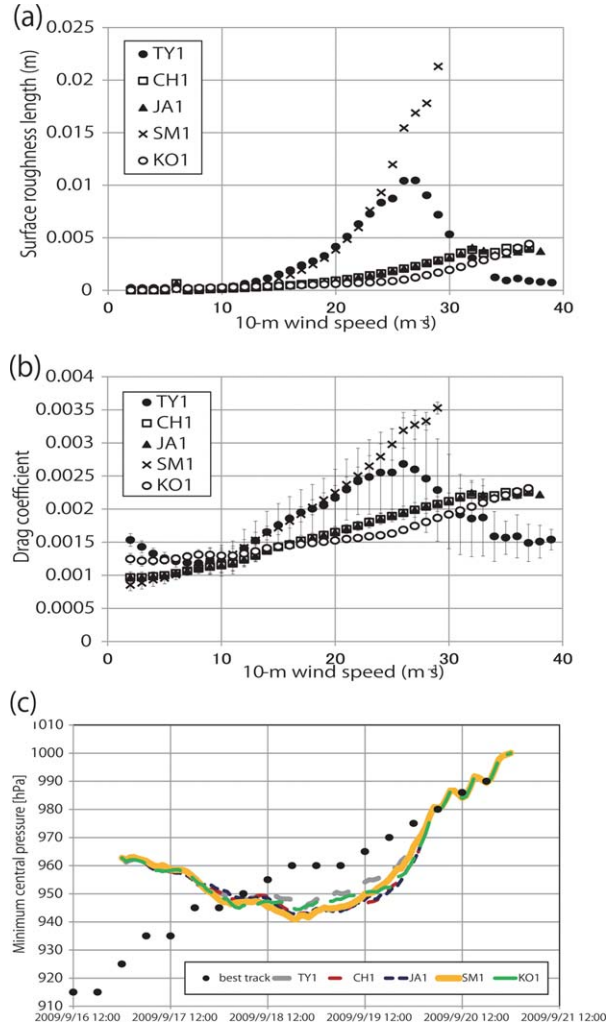

Figure 15. (a) Relation of 10 m wind speeds to surface roughness lengths at 72 h, (b) relation of 10 m wind speeds to drag coefficients at 72 h, and (c) time series plots of central pressure simulated in experiments TY1 (=C6G1), CH1, JA1, KO1, and SM1.

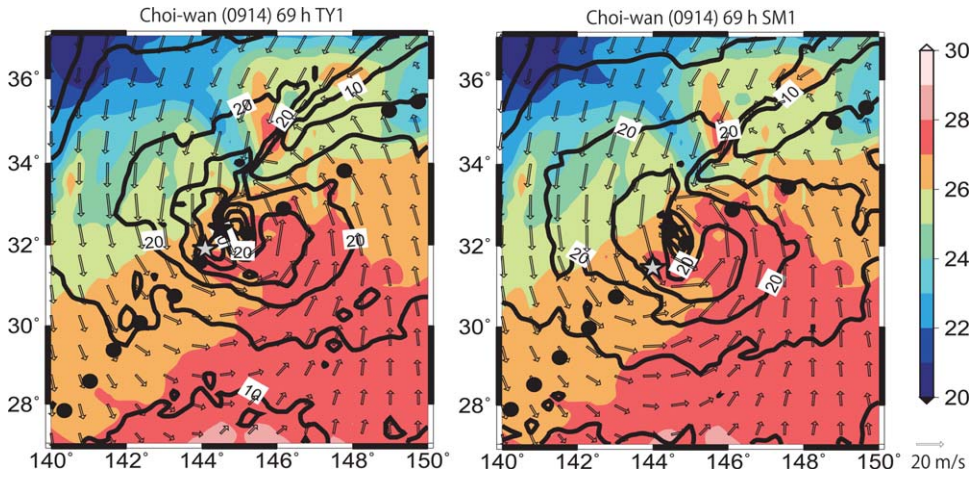

Figure 16. Horizontal distributions of SST (shades) and simulated 10 m wind speeds (vectors) at 69 h in (a) experiment TY1 (=C6G1) and (b) experiment SM1.

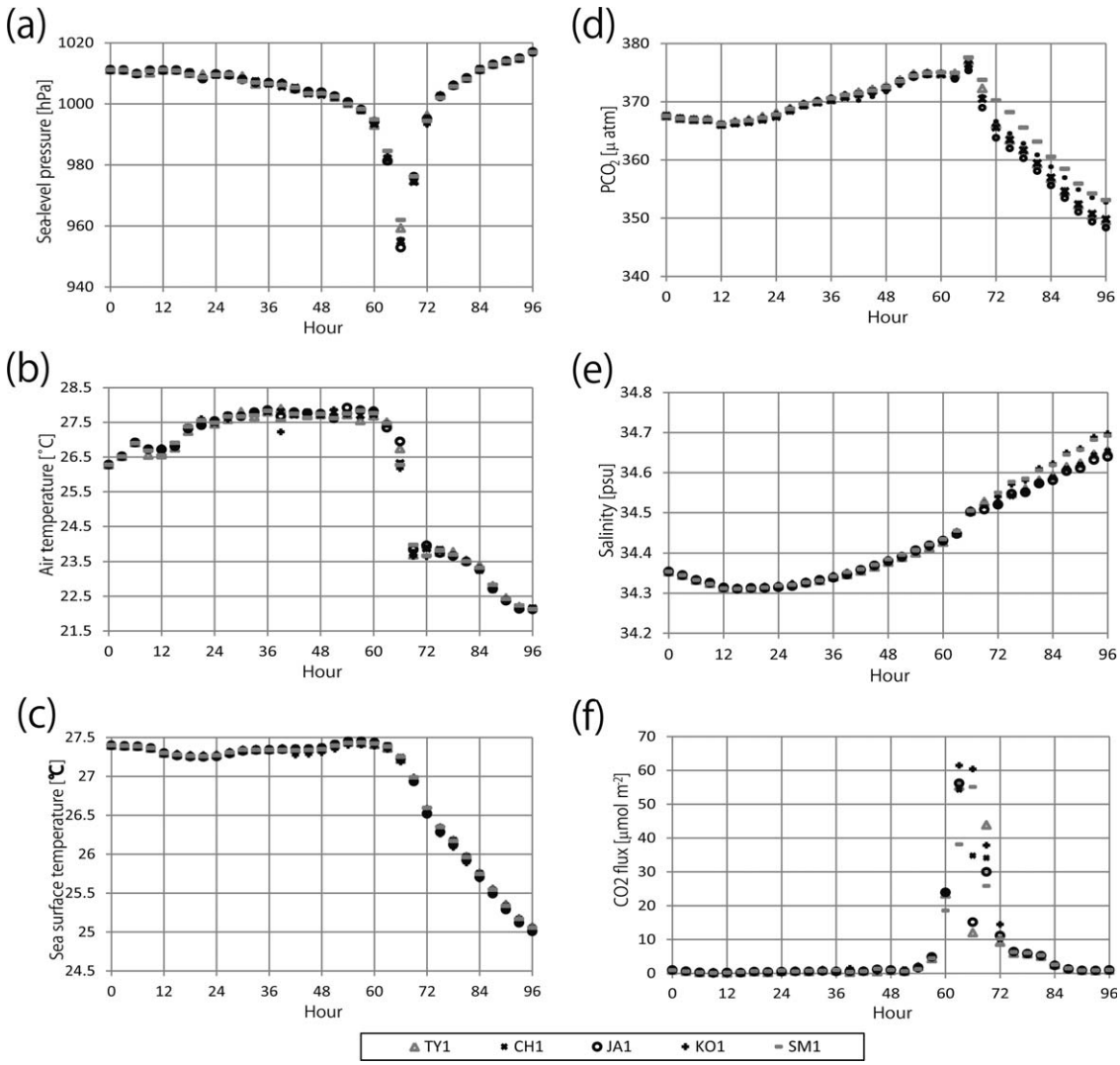

Figure 17. Time series plots of (a) sea-level pressure, (b) air temperature, (c) SST, (d) surface pCO_2^{sea} and normalized pCO_2^{sea} to a temperature of 29°C, (e) SSS, and (f) sea-air CO_2 flux simulated in experiments TY1 (=C6G1), CH1, JA1, KO1, and SM1. The location of model ingredients is 31.9°N, 144°E.

(Figure 1). Moreover, this study used a multilayer ocean model as the oceanic component of the coupled model. The multilayer ocean model may be insufficient to simulate the oceanic response to the typhoon even though the model can simulate near-inertial currents behind the typhoon to some extent [*Wada*, 2002]. *Bond et al*. [2011] showed that these asymmetrical winds generated strong inertial oscillations that can lead to mixing and sea-surface cooling even on the west side of the track. In order to simulate the oceanic response to the typhoon more precisely, a 3-D ocean general circulation model should be coupled to the atmosphere-wave-ocean coupled model instead of the multilayer model. Recently, ocean ecosystem models coupled with the 3-D ocean general circulation model has been used for investigating sea-air CO_2 flux [e.g., *Huang and Imberger*, 2010; *Xiu and Chai*, 2011; *Lévy et al*., 2012]. The development of the coupled model shown in Figure 1 will be a subject of a future study.

[55] Horizontal distributions of water temperature and salinity also can affect the variation in surface ocean pCO_2^{sea} at the KEO-moored buoy through horizontal and vertical advection. As described in the previous section, simulated water at the buoy was originated in cold, low-salinity water, which was engendered by heavy rainfall and vertical turbulent mixing caused by passage of seasonal rain front before the passage of Choi-wan. In addition, simulated high-salinity and DIC water occurred around 31.9°N, 144°E, south of the KEO-moored buoy, resulting in relatively high pCO_2^{sea}. This suggests that an oceanic horizontal field given at the initial time may be more important for reproducing local variation in surface pCO_2^{sea} at the KEO site by the coupled model than the initial vertical profiles of water temperature and salinity. We will conduct numerical experiments using more precise oceanic initial condition calculated by developed and more sophisticated assimilation method (e.g., 4-D variational estimation) or ensemble numerical simulations to evaluate the uncertainty. However, we also pay attention not only to the initial oceanic field but also to the variation in water temperature and salinity caused by ocean currents induced by passage of the typhoon.

[56] This study does not consider the effects of chlorophyll *a* variations on SST, DIC, and pCO_2^{sea} since the model is initialized with a climatological chlorophyll *a* created by *Kawai and Wada* [2011] and is assumed to be constant and vertically uniform during the entire integration time. The vertical profile of chlorophyll *a* is related to the computation of the penetration/absorption rate of solar radiation, which directly affects the vertical profile of water temperature in the upper ocean. Previous numerical studies [*Huang and Imberger*, 2010; *Wada et al*., 2011a] have shown that an increase in chlorophyll *a* due to the passage of a typhoon leads to a small increase in SST and pCO_2^{sea} a few days after the passage of a typhoon. To properly investigate this effect, a 3-D data set of chlorophyll *a* would be needed.

4.2. Surface Roughness Length, Typhoon Intensity and Structure, and Surface pCO_2

[57] This study shows in section 3.2.3 that surface pCO_2^{sea} during the passage of Choi-wan was sensitive to surface roughness length. In particular, resultant changes in the drag coefficient under high winds led to changes in coupled ocean-atmosphere processes within the inner core of simulated typhoon. The changes resulted in changes in surface wind speed and asymmetry of surface wind pattern and thereby led to changes in sea-level pressure and air temperature, all of which led to changes in sea-air CO_2 flux during the simulated Choi-wan's passage (Figures 17a, 17b, and 17f). Surface friction impacts on simulated SSS and pCO_2^{sea} due to changes in evaporation, advection, and turbulent mixing appeared after the passage of the typhoon (Figures 17d and 17e). Thus, surface wind asymmetry affects the evaporation, advection, and vertical turbulent mixing during and after the passage of the typhoon.

[58] The temporal increase in simulated DIC at 66 h around 31.9°N, 144°E (Figure 12a) does not appear to be caused by a rapid increase in sea-to-air latent heat flux. Because there is no gradual increase in analyzed DIC at the KEO buoy (Figure 12a) before the passage of Choi-wan, the effect of sea-to-air latent heat flux would have resulted in a large increase in DIC in the simulation by the coupled model. However, there is no increase in simulated DIC at the location of the KEO-moored buoy even though air temperature and SST are comparable between the two locations. A gradual increase in simulated DIC around 31.9°N, 144°E is not caused by sea-to-air latent heat flux.

[59] The increases in simulated SSS and pCO_2^{sea} (Figure 17) are sensitive to the change in surface winds due to the change in surface roughness lengths. This suggests that the increases in surface ocean DIC (Figure 12a) and associated pCO_2^{sea} around 31.9°N, 144°E were caused by vertical turbulent mixing and horizontal and vertical advection induced by continuous strong winds in the simulation even after the passage of the typhoon. Because the translation speed of the simulated typhoon exceeded 9 m s^{-1} and the depth of the mixed layer was 30 m or deeper, the effect of upwelling induced by Choi-wan on simulated SSS, DIC, and pCO_2^{sea} is considered to be smaller than that of the near-inertial currents and vertical turbulent mixing [e.g., *Wada*, 2002], in contrast to traditional upwelling regions such as Peruvian upwelling in the equatorial eastern Pacific [*Ishii et al*., 2004]. Because sea-surface cooling observed at the KEO buoy was ~1°C, which was smaller than that simulated by the coupled model, horizontal advection including typhoon-induced near-inertial currents likely played a crucial role in the increase in simulated pCO_2^{sea} after the passage of the typhoon. If near-inertial currents were simulated more realistically, it would contribute to the variation in pCO_2^{sea} shorter than a half day, corresponding to a half period for near-inertial oscillations. However, as described in section 4.1, errors associated with imperfect oceanic initial fields would still remain.

[60] In summary, surface pCO_2^{sea} changes during the passage of a typhoon are difficult to simulate, even with a sophisticated atmosphere-wave-ocean coupled model, as they require better representation of 3-D oceanic and atmospheric physics, inclusion of atmospheric chemical and oceanic biological processes, and precise initial conditions and atmospheric forcing with a proper surface roughness-length scheme (Figure 1). Direct observations of the pCO_2^{air} and pCO_2^{sea} during and after the typhoon are critical for validating the numerical simulations and for better understanding these processes.

5. Concluding Remarks

[61] On 19 September 2009, the eye of Typhoon Choi-wan (International designation 0914) passed ~40 km to the southeast of the KEO surface mooring, located at 32.3°N, 144.5°E. This study addresses typhoon-ocean interactions at the KEO buoy with regard to Choi-wan's wake, the response of partial pressure of surface ocean CO_2 (pCO_2^{sea}) to Choi-wan, the impact of the oceanic response to Choi-wan on the intensity and surface wind asymmetry of Choi-wan, and roles of an oceanic field given at the initial time in the Choi-wan's simulations. This study was motivated by the observed rapid variation in the sea minus atmosphere partial pressure of CO_2 (ΔpCO_2) observed by the KEO mooring during the passage of Choi-wan [*Bond et al*., 2011].

[62] An atmosphere-wave-ocean coupled model [*Wada et al*., 2010] incorporating an oceanic carbon equilibrium scheme developed by *Wada et al*. [2011a] was used to investigate these interactions. The horizontal resolution of the coupled model is 6 km, and no cumulus parameterization is used in the series of numerical experiments. The initial time of numerical simulation is 0000 UTC on 17 September 2009, corresponding to the mature phase of Choi-wan. The atmospheric initial condition is provided from the JMA six hourly global objective analysis data with a horizontal resolution of 20 km. Oceanic initial and boundary conditions are derived from the MOVE system, forced with daily oceanic reanalyses. In order to investigate the impact of the horizontal resolution, two initialization fields are created: one with a large scale grid with 0.5° resolution and one with a regional scale grid with 0.1° resolution [*Usui et al*., 2006].

[63] First of all, the track simulation is reasonably close to the best track although the translation speed of ~10.5 m s^{-1} is ~3 m s^{-1} slower than that of the best track (~13.8 m s^{-1}) when the typhoon passes near the buoy at 1800 UTC on 18 September. Sea-surface cooling induced by Choi-wan helps weaken Choi-wan's intensity. As a consequence, the evolution of sea-level pressure observed at the KEO-moored buoy compares better in the simulated-typhoon reference frame with that of a grid point to the southwest at 31.9°N, 144°E, which is northwest of the simulated-typhoon eye at 66 h. In situ observations show CO_2 outgassing during the passage of Choi-wan. Approximately 60% of ΔpCO_2 reported by *Bond et al*. [2011] is explained by a rapid increase of surface ocean pCO_2^{sea} during the typhoon passage, and 40% is explained by a rapid decrease of pCO_2^{air}.

[64] The numerical simulations also show that changes in near-inertial currents and vertical turbulent mixing due to a slow translation speed, excessive intensity of simulated typhoon, and the resultant simulated oceanic field including the oceanic response to simulated stagnant seasonal rain front lead to excessive low simulated SST, salinity, and DIC at the KEO buoy site and thereby an excessive decrease in pCO_2^{sea} after the passage of the typhoon. We investigate the effect of the physical and carbonic ocean response to Choi-wan on an increase in surface pCO_2^{sea} after the passage of the typhoon. At the grid point at 31.9°N, 144°E in the simulated-typhoon reference frame, this study roughly simulates an increase in pCO_2^{sea}, but the value (~9.6 μatm) corresponds to only roughly 20% of the ΔpCO_2 change, one third of the increase in observed pCO_2^{sea}. The present study is the first to show that not only SST but also high salinity and DIC caused by vertical turbulent mixing and near-inertial currents are important in simulating surface pCO_2^{sea} variation.

[65] This study also reveals that a change of surface roughness-length scheme directly affects the simulated sea-level pressure, air temperature, and sea-air CO_2 flux at the location of the KEO buoy during the passage of Choi-wan and has an effect on the variations in SSS after the passage of the typhoon and pCO_2^{sea} during and after the passage of the typhoon. The change of surface roughness-length scheme also affects the surface wind asymmetry but has little effect on sea-surface cooling induced by Choi-wan. Strong surface friction plays a role in intensification of Choi-wan, while it enables weakening of the typhoon during the mature phase. Therefore, the effect of a change of surface roughness-length scheme on pCO_2^{sea} may differ depending on the phase of the typhoon.

[66] While the coupled atmosphere-ocean-wave model with atmospheric chemical and biogeochemical component is ideal for studying the interdisciplinary nature of a typhoon, the added complexity, and particularly the uncertainties associated with the various elements, is challenging. Having high-resolution in situ observations from the KEO buoy was critical for validating and interpreting the results of the simulations. We hope that this study will contribute to the development of more sophisticated coupled model and multidisciplinary research.

[67] **Acknowledgments.** The authors are grateful to two anonymous reviewers for comments that helped to improve this manuscript. The authors thank N. Usui for providing oceanic reanalysis data and helpful comments. A.W. was supported by fund from the Japan Society for the Promotion of Science (JSPS) KAKENHI grant 22540454 and by the Japanese Ministry of Education, Culture, Sports, Science and Technology (MEXT) KAKENHI grant 23106505. The Generic Mapping Tools (http://gmt.soest.hawaii.edu/) was used to draw figures.

References

Bates, N. R., A. H. Knap, and A. F. Michaels (1998), Contribution of hurricanes to local and global estimates of air-sea exchange of CO2, *Nature*, *395*, 58–61, doi:10.1038/25703.

Bender, M. A., and I. Ginis (2000), Real-case simulations of hurricane-ocean interaction using a high-resolution coupled model: Effects on hurricane intensity. *Mon. Weather Rev.*, *128*, 917–946. doi:10.1175/1520-0493(2000)128<0917:RCSOHO>2.0.CO;2.

Bender, M. A., I. Ginis, and Y. Kurihara (1993), Numerical simulations of the tropical cyclone-ocean interaction with a high-resolution coupled model, *J. Geophys. Res.*, *98*, 23,245–23,263. doi:10.1029/93JD02370.

Bond, N. A., M. F. Cronin, C. Sabine, Y. Kawai, H. Ichikawa, P. Freitag, and K. Ronnholm (2011), Upper ocean response to Typhoon Choi-wan as measured by the Kuroshio Extension Observatory mooring, *J. Geophys. Res.*, *116*, C02031, doi:10.1029/2010JC006548.

Charnock, H. (1955), Wind stress on a water surface, *Q. J. R. Meteorol. Soc.*, *81*, 639–640, doi:10.1002/qj.49708135027.

Cronin, M. F., C. Meinig, C. L. Sabine, H. Ichikawa, and H. Tomita (2008), Surface mooring network in the Kuroshio Extension, *IEEE Syst. J.*, *2*(3), 424–430, doi:10.1109/JSYST.2008.925982.

Cronin, M. F., N. A. Bond, J. T. Farrar, H. Ichikawa, S. R. Jayne, Y. Kawai, M. Konda, B. Qiu, L. Rainville, and H. Tomita (2013), Formation and erosion of the seasonal thermocline in the Kuroshio Extension recirculation gyre, *Deep Sea Res. Part II*, *85*, 62–74, doi:10.1016/j.dsr2.2012.07.018.

Deardorff, J. W. (1980), Stratocumulus-capped mixed layers derived from a three-dimensional model, *Boundary Layer Meteorol.*, *18*, 495–527, doi:10.1007/BF00119502.

Deardorff, J. W. (1983), A multi-limit mixed-layer entrainment formulation, *J. Phys. Oceanogr.*, *13*, 988–1002, doi:10.1175/1520-0485(1983)013<0988:AMLMLE>2.0.CO;2.

Dickson, A. G., C. L. Sabine, and J. R. Christian (2007), Guide to best practices for ocean CO2 measurements. PICES Spec. Publ. 3, 191 pp., *Carbon Dioxide Inf. Anal. Cent.*, Oak Ridge Natl. Lab., Oak Ridge, Tenn.

Dvorak, V. F., (1975), Tropical cyclone intensity analysis and forecasting from satellite imagery, *Mon. Weather Rev.*, *103*, 420–430.

Huang, P., and J. Imberger (2010), Variation of pCO2 in ocean surface water in response to the passage of a hurricane. J. Geophys. Res., *115*, C*10024*, doi:10.1029/2010JC006185.

Ishii, M., S. Saito, T. Tokieda, T. Kawano, K. Matsumoto, and H. Y. Inoue (2004), *Variability of surface layer CO_2 parameters in the western and central equatorial Pacific*, in Global Environmental Change in the Ocean and on Land, edited by M. Miyoshi et al., TERRAPUB, Japan pp. 59–94.

Janssen, P. A. E. M. (1991), Quasi-linear theory of wind-wave generation applied to wave forecasting. J. Phys. Oceangr., *21*, *1631–1642*, doi:10.1175/1520-0485(1991)021<1631:QLTOWW>2.0.CO;2.

Kamahori, H., N. Yamazaki, N. Mannoji, and K. Takahashi (2006), Variability in intense tropical cyclone days in the western North Pacific, *SOLA*, *2*, 104–107, 10.2151/sola.2006-027.

Kawai, Y., and A. Wada (2011), Detection of cyclone-induced rapid increases in chlorophyll-a with sea surface cooling in the northwestern Pacific Ocean from a MODIS/SeaWiFS merged satellite chlorophyll product. Int. J. Remote Sens., *32*, *9455–9471*, doi:10.1080/01431161.2011.562252.

Klemp, J. B., and R. Wilhelmson (1978), The simulation of three-dimensional convective storm dynamics, *J. Atmos. Sci.*, *35*, 1070–1096, doi:10.1175/1520-0469(1978)035<1070:TSOTDC>2.0.CO;2.

Knapp, K. R., M. C. Kruk, D. H. Levinson, H. J. Diamond, and C. J. Neumann (2010), The International Best Track Archive for Climate Stewardship (IBTrACS): Unifying tropical cyclone best track data, *Bull. Am. Meteorol. Soc.*, *91*, 363–376, doi:10.1175/2009BAMS2755.1.

Kondo, J. (1975), Air-sea bulk transfer coefficients in diabatic conditions, *Boundary Layer Meteorol.*, *9*, 91–112, doi:10.1007/BF00232256.

Lévy, M., M. Lengaigne, L. Bopp, E. M. Vincent, G. Madec, C. Ethé, D. Kumar, and V. V. S. S. Sarma (2012), Contribution of tropical cyclones to the air-sea CO2 flux: A global view, *Global Biogeochem. Cycles*, *26*, GB2001, doi:10.1029/2011GB004145.

Lin, I.-I. (2012), Typhoon-induced phytoplankton blooms and primary productivity increase in the western North Pacific subtropical ocean, *J. Geophys. Res.*, *117*, C03039, doi:10.1029/2011JC007626.

Lin, I.-I, W. T. Liu, C.-C. Wu, G. T. F. Wong, C. Hu, Z. Chen, W.-D. Liang, Y. Yang, and K.-K. Liu (2003), New evidence for enhanced ocean primary production triggered by tropical cyclone, *Geophys. Res. Lett.*, *30*(13), 1718, doi:10.1029/2003GL017141.

Lin, Y. H., R. D. Farley, and H. D. Orville (1983), Bulk parameterization of the snow field in a cloud model, *J. Clim. Appl. Meteorol.*, *22*, 1065–1092, doi:10.1175/1520-0450(1983)022<1065:BPOTSF>2.0.CO;2.

Louis, J. F., M. Tiedtke, and J. F. Geleyn (1982), *A short history of the operational PBL parameterization at ECMWF*, in Proceedings of Workshop on Planetary Boundary Layer Parameterization, pp. 59–79, ECMWF, Reading, U. K.

Nemoto, K., T. Midorikawa, A. Wada, K. Ogawa, S. Takatani, H. Kimoto, M. Ishii, H. Y. Inoue (2009), Continuous observations of atmospheric and oceanic CO2 using a moored buoy in the East China Sea: Variations during the passage of typhoons, *Deep Sea Res. Part II*, *56*, 542–553, doi:10.1016/j.dsr2.2008.12.015.

Ohlmann, J. C., and D. A. Siegel (2000), Ocean radiant heating. Part II: Parameterizing solar radiation transmission through the upper ocean, *J. Phys. Oceanogr.*, *30*, 1849–1865, doi:10.1175/1520-0485(2000)030<1849:ORHPIP>2.0.CO;2.

Powell, M., P. Vickery, and T. Reinhold (2003), Reduced drag coefficients for high wind speeds in tropical cyclones, *Nature*, *422*, 279–283, doi:10.1038/nature01481.

Price, J. F. (1981), Upper ocean response to a hurricane, *J. Phys. Oceanogr.*, *11*, 153–175, doi:10.1175/1520-0485(1981)011<0153:UORTAH>2.0.CO;2.

Price, J. F. (1983), Internal wave wake of a moving storm. Part I: Scales, energy budget and observations, *J. Phys. Oceanogr.*, 13, 949–965.

Saito, K. (2012), The JMA Nonhydrostatic model and its applications to operation and research, in *Atmospheric Model Applications*, pp. 85–110, InTech, Croatia, doi:10.5772/35368.

Sarrat, C., et al. (2007), Atmospheric CO2 modeling at the regional scale: an intercomparison of 5 meso-scale atmospheric model, *Biogeosciences*, *4*, 1115–1126.

Schiller, A., and J. S. Godfrey (2005), A diagnostic model of the diurnal cycle of sea surface temperature for use in coupled ocean-atmosphere models, *J. Geophys. Res.*, *110*, C11014, doi:10.1029/2005JC002975.

Siswanto, E., J. Ishizaka, A. Morimoto, K. Tanaka, K. Okamura, A. Kristijono, and T. Saino (2008), Ocean physical and biogeochemical responses to the passage of Typhoon Meari in the East China Sea observed from Argo float and multiplatform satellites, *Geophys. Res. Lett.*, *35*, L15604, doi:10.1029/2008GL035040.

Smith, S. D., et al. (1992), Sea surface wind stress and drag coefficients: The HEXOS results. *Boundary Layer Meteorol.*, *60*, 109–142, doi:10.1007/BF00122064.

Subrahmanyam, B., K. H. Rao, N. Srinivasa Rao, V. S. N. Murty, and R. J. Sharp (2002), Influence of a tropical cyclone on chlorophyll-a concentration in the Arabian Sea, *Geophys. Res. Lett.*, *29*(22), 2065, doi:10.1029/2002GL015892.

Sugi, M., K. Kuma, K. Tada, K. Tamiya, N. Hasegawa, T. Iwasaki, S. Yamada, and T. Kitade (1990), Description and performance of the JMA operational global spectral model (JMA-GSM88), *Geophys. Mag.*, *43*, 105–130.

Taylor, P. K., and M. J. Yelland (2001), The dependence of sea surface roughness on the height and steepness of the waves. *J. Phys. Oceanogr.*, *31*, 572–590, doi:10.1175/1520-0485(2001)031<0572:TDOSSR>2.0.CO;2.

Usui, N., S. Ishizaki, Y. Fujii, H. Tsujino, T. Yasuda, and M. Kamachi (2006), Meteorological Research Institute multivariate ocean variational estimation (MOVE) system: Some early results, *J. Adv. Space Res.*, *37*, 806–822, doi:10.1016/j.asr.2005.09.022.

Wada, A. (2002), The processes of SST cooling by typhoon passage and case study of Typhoon Rex with a mixed layer ocean model, *Pap. Met. Geophys.*, *52*, 31–66, doi:10.2467/mripapers.52.31.

Wada, A. (2009), Idealized numerical experiments associated with the intensity and rapid intensification of stationary tropical-cyclone-like vortex and its relation to initial sea-surface temperature and vortex-induced sea-surface cooling, *J. Geophys. Res.*, *114*, D18111, doi:10.1029/2009JD011993.

Wada, A. (2010), *Tropical-cyclone-ocean interaction: Numerical studies, in Advances in Energy Research, vol. 1*, edited by M. J. Acosta, pp. 1–67, NOVA Sci., Hauppauge, New York.

Wada, A. (2012), Numerical study on the effect of the ocean on tropical-cyclone intensity and structural change, *in Atmospheric Model Applications*, pp. 43–68, InTech, Croatia, doi:10.5772/34418.

Wada, A., and N. Usui (2010), Impacts of oceanic preexisting conditions on predictions of Typhoon Hai-Tang in 2005, *Adv. Meteorol.*, 2010, 15 pp., doi:10.1155/2010/756071.

Wada, A., H. Niino, and H. Nakano (2009), Roles of vertical turbulent mixing in the ocean response to Typhoon Rex (1998), *J. Oceanogr.*, *65*, 373–396, doi:10.1007/s10872-009-0034-8.

Wada, A., N. Kohno, and Y. Kawai (2010), Impact of wave-ocean interaction on Typhoon Hai-Tang in 2005, *SOLA*, *6A*, 13–16, 10.2151/sola.6A-004.

Wada, A, T. Midorikawa, M. Ishii, and T. Motoi (2011a), Carbon system changes in the East China Sea induced by typhoons Tina and Winnie in 1997, *J. Geophys. Res.*, *116*, C07014, doi:10.1029/2010JC006701.

Wada, A., T. Midorikawa, and M. Ishii (2011b), Rapid decreases in CO2 during the passage of Tina and Winnie (1997), *CAS/JSC WGNE Res. Activ. Atmos. Oceanic Modell. Rep. 41*, pp. 8.03–8.04, WMO, Geneva, Switzerland.

Wanninkhof, R. (1992), Relationship between wind speed and gas exchange over the ocean, *J. Geophys. Res.*, *97*(C5), 7373–7382, doi:10.1029/92JC00188.

Wu, L., B. Wang, and S. A. Braun (2005), Impact of air-sea interaction on tropical cyclone track and intensity, *Mon. Weather Rev.*, *133*, 3299–3314, doi:10.1175/MWR3030.1.

Xiu, P., and F. Chai (2011), Modeled biogeochemical responses to meso-scale eddies in the South China Sea, *J. Geophys. Res.*, *116*, C10006, doi:10.1029/2010JC006800.

Zhu, H., W. Ulrich, and R. K. Smith (2004), Ocean effects on tropical cyclone intensification and inner-core asymmetries, *J. Atmos. Sci.*, *61*, 1245–1258, doi:10.1175/1520-0469(2004)061<1245:OEOTCI>2.0.CO;2.